Journal of the Brazilian Society of Mechanical Sciences and Engineering (2019) 41:484
https://doi.org/10.1007/s40430-019-1989-z

TECHNICAL PAPER

A methodology for the performance prediction: flow field and thermal analysis of a helium turboexpander

Manoj Kumar[1] · **Debashis Panda**[1] · **Amitesh Kumar**[2] · **Ranjit K. Sahoo**[1] · **Suraj K. Behera**[1]

Received: 24 July 2019 / Accepted: 26 September 2019 / Published online: 11 October 2019

Abstract

Helium liquefaction systems are widely used in nuclear fission, superconductivity, space industries, and other scientific instruments. However, the efficiency of these systems is quite low due to the cryogenic operating temperature. In this regard, the one-dimensional design methodology of the helium turbine and nozzle (hereafter, renowned as turboexpander) is important to increase the efficiency of the system. This paper demonstrates the sensitivity analysis and optimal range of non-dimensional design variables on which the radial inflow turbine has maximum efficiency, minimum losses, and maximum power output using artificial intelligence techniques. On this basis, three turboexpander models are developed within the optimal range of predicted non-dimensional variables. After that, a comparative numerical study is carried out to highlight the flow field and thermal characteristics of helium fluid. The standard two equations $k{-}\omega$ SST model is used to solve the three-dimensional incompressible flow inside the computational domain. The numerical results are validated with the available experimental data from the existing literature. The variation of Mach number, Reynolds number, Prandtl number, static entropy, static enthalpy, temperature, and pressure inside the turboexpander is significantly affected by blade profile which is enormously affected by the design methodology. The study also demonstrates the flow separation region, vortex formation, tip leakage flow, secondary losses, and its reasons along with the spanwise location. The results highlight the importance of the design methodology, sensitivity analysis, the prediction capability of the artificial intelligence network, numerical methodology, and development of the helium turboexpander prototype models.

Keywords Helium turboexpander · Sobol sensitivity analysis · Flow pattern · Thermal characteristics · Artificial intelligence

List of symbols

b	Blade height (m)
b_t	Nozzle height (m)
C	Absolute velocity (m/s)
C_0	Spouting velocity (m/s)
Ch_n	Chord length (m)
C_{mt}	Nozzle throat velocity (Meridional component) (m)
$C_{\theta t}$	Nozzle throat velocity (Tangential component) (m)
c_p	Specific heat capacity (J/kg K)
D	Turbine diameter ratio
D_h	Hydraulic diameter (m)
D_n	Diameter of nozzle ring (m)
D_t	Nozzle throat circle diameter (m)
$D_i(Y)$	First-order variance
$D_{ij}(Y)$	Second-order variance
d_s	Specific diameter
h	Enthalpy (kJ/kg)
k_0	Thermal conductivity of fluid (W/mK)
L_t	Total loss
$\dot{m}$	Mass flow rate (kg/s)
n_s	Specific speed
P	Power (kW)
p	Pressure (Pa)
R_2	Turbine inlet radius (m)
R_h	Hub radius (m)
R_s	Shroud radius (m)
r_p	Pressure ratio
S_i	First-order sensitivity index

Technical Editor: Erick de Moraes Franklin, Ph.D.

✉ Manoj Kumar
manojbeg526@gmail.com

[1] National Institute of Technology Rourkela, Rourkela, Odisha 769008, India

[2] Indian Institute of Technology Varanasi, Varanasi, U.P 221005, India

U	Mean flow velocity (m/s)
u	Blade speed (m/s)
$\mathrm{Var}(Y)$	Total variance of the output
v_s	Velocity ratio
W	Relative velocity (m/s)
W_t	Throat width (m)
X	Parameters
x_i	Number of inputs
Y	Target function
Z	Number of blades
Z_r	Rotor axial length (m)

Greek symbols

α	Absolute flow angle $(\circ)$
β	Relative flow angle $(\circ)$
ζ_b	Back friction
ζ_l	Leakage loss
ε_x	Axial clearance (m)
ε_r	Radial clearance (m)
λ	Ratio of rotor outlet to inlet
μ	Coefficient of viscosity (Pa s)
Ω	Degree of reaction
ρ	Density $\mathrm{kg/m^3}$
ψ_z	Zweifel number
ϕ	Flow coefficient
ψ	Stage loading coefficient
χ	Absolute meridional velocity
η_{is}	Isentropic efficiency
ω	Rotational speed (rpm)

Subscripts

1	Nozzle inlet
2	Turbine inlet
3	Rotor outlet
h	Hub
m	Meridional
n	Nozzle
r	Radial
s	Shroud
t	Throat
z	Axial
θ	Tangential

Abbreviations

ANFIS	Adaptive neuro-fuzzy inference system
ANN	Artificial neural network
GA	Genetic algorithms
HEX	Heat exchanger
MAE	Mean absolute error
MF	Membership function
MLP	Multilayer perceptron
ORC	Organic Rankine cycle
PS	Pressure surface
RMSE	Root-mean-squared error
SS	Suction surface
SST	Shear stress transport
TF	Transfer function
TKE	Turbulence kinetic energy

1 Introduction

Cryogenic turboexpanders are employed to produce the ultra-low temperature, which are beneficial in different fields such as space applications, superconductivity, industrial applications, and biomedical and chemical instruments [1]. The development of large-scale cryogenic systems operating at liquid helium temperature is used in the field of nuclear fusion and high-energy physics [2]. Some recognized international research centers like Large Hadron Collider (LHC), the ITER, and the National Advanced Experimental Superconducting Tokamak are based on helium cryogenic systems and need a huge amount of liquid helium. The demand can be fulfilled by using a Collins cycle based turboexpander system. The energy consumption of these systems is significant at ultra-low temperature. Therefore, small increment in turboexpander efficiency has a significant effect on the performance of the system.

Researchers suggest that the radial inflow turbines are best suited for the cryogenic turboexpander, aircraft power units, and other industrial applications due to its higher efficiency, compact size, low manufacturing cost, and relatively easy design process as compared to axial turbines [3–5]. Therefore, the optimal design methodology of these components is necessary for higher thermal efficiency of the system and a matter of interest among the research community [6]. Also, the aforementioned specialty enforces the usage of these types of turbine where the high-pressure ratio (above 2) is required, and the size of the turbine is another constraint. Generally, the pressure ratio across the turbine depends on the thermodynamic boundary conditions, i.e., pressure and temperature at inlet, outlet, and working fluid as well. Some available literature for high-pressure ratio turbines is mentioned in Table 1. Aungier [7] proposed the most celebrated one-dimensional design methodology for radial inflow turbine.

The efficiency of small-scale radial turbine can be increased by minimizing the losses. The impeller back friction, incidence, blade loading, and leakage loss are essential to be considered in the design process of helium turbine for cryogenic applications [15]. These losses depend on some non-dimensional design variables which must be optimized for better performance of the turbine. For this purpose, artificial neural network (ANN) and adaptive neuro-fuzzy inference system (ANFIS) are used due to its better prediction capability, fast response, reliability, and computationally less expensive [16–19]. Moraal and Kolmanovsky [20] suggest

Table 1 Radial inflow turbine design and testing summary

Authors	Field	Pressure ratio	Fluid
Ino et al. [8]	Cryogenics	7.0–12.0	Helium
Ghosh [9]	Cryogenics	1.8–6.0	Air
Balaji [10]	Cryogenics	2.0–5.8	Air
Larjola [11]	ORC	10.0	R114
Kumar et al. [12]	Cryogenics		Air
Sam et al. [13]	Cryogenics	1.5	Helium
Pei et al. [14]	ORC	7.0	R123
Li et al. [15]	Cryogenics	5.53	Helium

that ANN is superior to the curve fitting approach for optimizing the turbine geometry. These models can also combine with genetic algorithms (GA) to optimize the design parameters of different components [21]. Several researchers report the usage of ANN and ANFIS model for performance prediction of gas turbines. Some of them apply this methodology in turbomachinery as well as to investigate the performance of gas turbines, and compressors [22–25]. Kong et al. [26, 27] use GA and neural network to obtain the variables on which the performance of a compressor depends.

The exact analysis of the flow field and thermal characteristics of the turboexpander can be obtained from the experimental investigation. But, it is extremely difficult and cost-effective to develop such type of experimental setup at cryogenic temperature using helium as a working fluid. In recent decades, the evolution of numerical techniques overcomes these issues [28, 29]. It is also beneficial to characterize the flow field and thermal behavior at different points inside the turboexpander which is extremely difficult in experiments. Sam et al. [30] investigate the design and flow field analysis of a high-pressure helium turboexpander for Claude-based liquefaction cycles. They discuss the effect of geometrical variables on the design methodology and performance of the turboexpander. Kushwaha and Bora [31] design a mixed flow turbine for helium turboexpander using similarity principles. Some remarkable numerical works are reported on aerodynamic investigations of high-pressure ratio turbine [32, 33].

Literature review illustrates that there are some mathematical models available for predicting the performance of radial turbine, but none of them report the variation of isentropic efficiency, total loss, and power output with the non-dimensional design variables for cryogenic helium turbine using artificial intelligence technique. Also, a comparative numerical analysis of fluid flow and thermal characteristics of high-, medium- and low-pressure turboexpander are missing in the existing literature. The present work reports fulfilling this literature gap.

In this paper, the one-dimensional design methodology of a radial inflow turbine and nozzle are proposed considering the effect of different loss models. Sobol sensitivity analysis is carried out to study the effect of major non-dimensional variables on the performance of turbine. The optimal range of these variables is predicted by developing the artificial neural network (ANN) and adaptive neuro-fuzzy inference system (ANFIS) model. Finally, three turboexpander models are designed for three different operating conditions. Furthermore, three-dimensional numerical simulations are conducted to visualize the fluid flow and thermal characteristics of the designed turboexpander using helium (real gas) as a working fluid.

The paper is systemized as follows: Section 2 illustrates the design methodology of the turbine and nozzle considering loss models and Sobol sensitivity analysis to identify the important design variables; Sect. 3 illustrates the development of ANN and ANFIS network and their predicted results; Sect. 4 illustrates the numerical methodology, boundary conditions, and grid independence study; Sect. 5 reports the experimental validation and important findings; Sect. 6 concludes the results.

2 Preliminary design procedure

2.1 An approach to design a helium turboexpander system

Figure 1 illustrates the design of a helium turboexpander system based on Collins cycle. The system consists of a helium compressor, cryogenic valves, cryogenic helium turboexpanders (high, medium, and low pressure), heat exchangers, reservoir, etc. The helium is compressed from atmospheric pressure to high pressure (17 bar), and then precooled in the HEX 1 which is equipped with liquid nitrogen. In this way, the high-pressure (16 bar and 80 K) helium passes through the high-pressure turboexpander ($T1$). The outlet pressure is maintained to be 8 bar to decrease the irreversibility of the system. The temperature drop in the first stage expansion is approximately 17 K. To overcome the turbulence and vortices at the outlet of the first stage expansion, HEX 2 is placed in which the subcooling of the fluid takes place. After that, the fluid (8 bar, 60 K) passes through medium-pressure turboexpander ($T2$). In this stage, 14 K temperature drop is achieved. In the last stage of expansion, 12 K temperature drop takes place. After the expansion through the low-pressure turboexpander ($T3$), the pressure and temperature of the fluid are 2 bar and 37 K. In this way, approximately 43 K temperature drop is achieved during the one complete process. The Joule–Thomson valve is placed after the HEX 3, and the process is repeated.

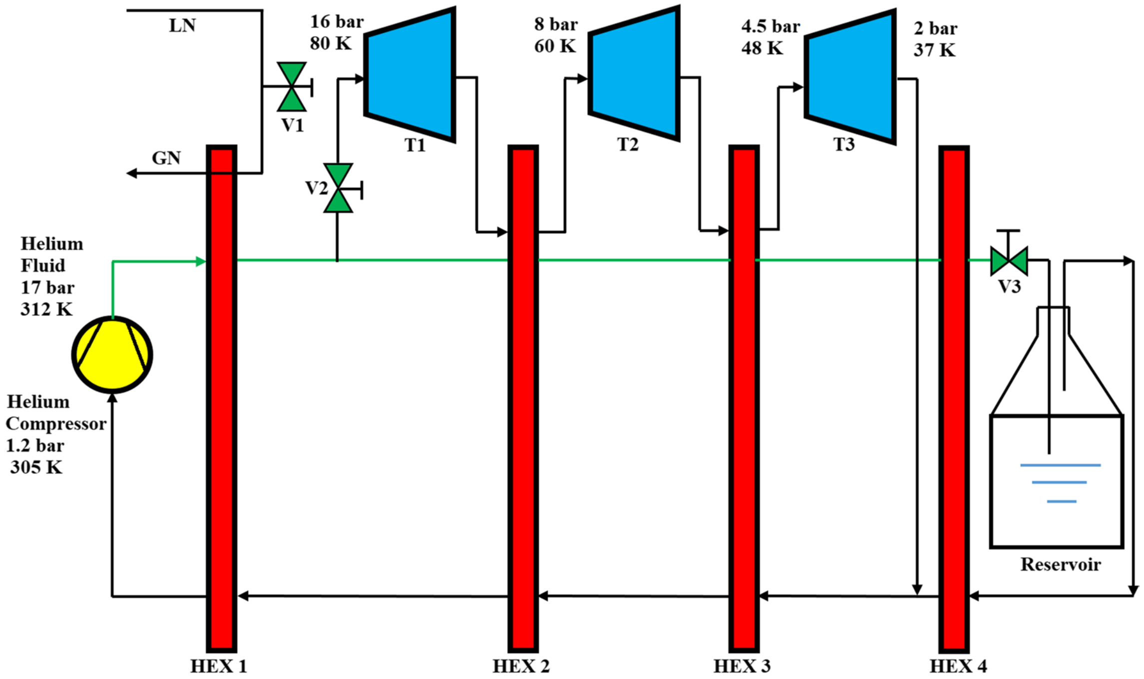

Fig. 1 Schematic diagram of helium liquefaction cycle

2.2 Preliminary design of radial inflow turbine

The aforementioned analysis prescribes the necessity of efficient helium turbine to maximize the system performance. In this regard, the one-dimensional design methodology of a radial inflow turbine is introduced by adopting the analytical approach proposed by Hasselgruber and Balje using the underlying primary data (thermodynamic properties) and non-dimensional parameters in MATLAB® 2017b. Generally, the cryogenic fluids are diatomic gas, and its thermophysical properties are significantly varied at high-pressure and ultra-low temperature. Also, the turbine used in such kind of system must possess a low mass flow rate and higher enthalpy drop. Due to this, the thermophysical properties of the working fluid have a significant effect on the aerodynamic design of the radial inflow turbine [34]. Therefore, the thermodynamic state needs real gas properties which are obtained from REFPROP [15].

In the design process, inlet pressure (p), mass flow rate ($\dot{m}$), pressure ratio $\left(r_{\mathrm{p}}\right)$, rotational speed ($\omega$), blade speed ratio, flow angles and a number of blades (Z), etc. are the decision variables on which the performance of the turbine depends. Velocity ratio $\left(v_{\mathrm{s}}\right)$, degree of reaction ($\Omega$), turbine diameter ratio (D), and the number of blades (Z) are other parameters on which the feasibility of the turbine design depends. The ranges of different parameters are mentioned in Table 2.

In the design process of a radial-type turbine, machining precisions are carefully considered; therefore, low values of the degree of reaction are taken. To maintain the flow in the subsonic region, stage loading (ψ) and flow coefficient (ϕ) values are taken to be higher. The first step is to select the degree of reaction (Ω), stage loading, and flow coefficient.

Table 2 Ranges of different parameters of radial turbine design for cryogenic applications

Design variables		Other reasonable variables	
$\dot{m}$ (kg/s)	0.01–0.09	Velocity ratio $\left(v_{\mathrm{s}}\right)$	0.62–0.74
Tip clearance	0.1	R_{s}/R_2	0.85–0.96
ω (rpm) (Million)	0.14–0.25	R_{h}/R_2	0.22–0.26
L/D	0.35–0.46	r_{p}	1.4–3.5
Blade speed ratio	0.60–0.82	Specific speed $\left(n_{\mathrm{s}}\right)$	0.482–0.596
Blade inlet angle (°)	72–82	Specific diameter $\left(d_{\mathrm{s}}\right)$	2.81–3.38
Blade exit angle (°)	− 2.8 to − 3.6		
Z	8–17		

$$\phi = \frac{C_{m3}}{u_2} = \frac{C_{m2}}{\chi u_2} \tag{1}$$

$$\psi = \frac{\triangle h_0}{u_2^2} = \frac{C_{\theta 2}}{u_2} - \lambda \frac{C_{\theta 3}}{u_2} \tag{2}$$

where χ represents the absolute meridional velocity at the inlet and outlet of the rotor and λ is the outlet to inlet radius ratio of the turbine.

Power output,

$$P = \dot{m}\left(h_2 - h_3\right) \tag{3}$$

In the design process of helium turbine, the back friction $\left(\zeta_b\right)$ and leakage loss $\left(\zeta_l\right)$ are considered [15]. The isentropic efficiency $\left(\eta_{is}\right)$ of the turbine is updated in one-dimensional design procedure. Figure 2 illustrates the one-dimensional design approach of a radial inflow turbine. The velocity triangles and geometrical specifications of a radial inflow turbine are represented in Fig. 3.

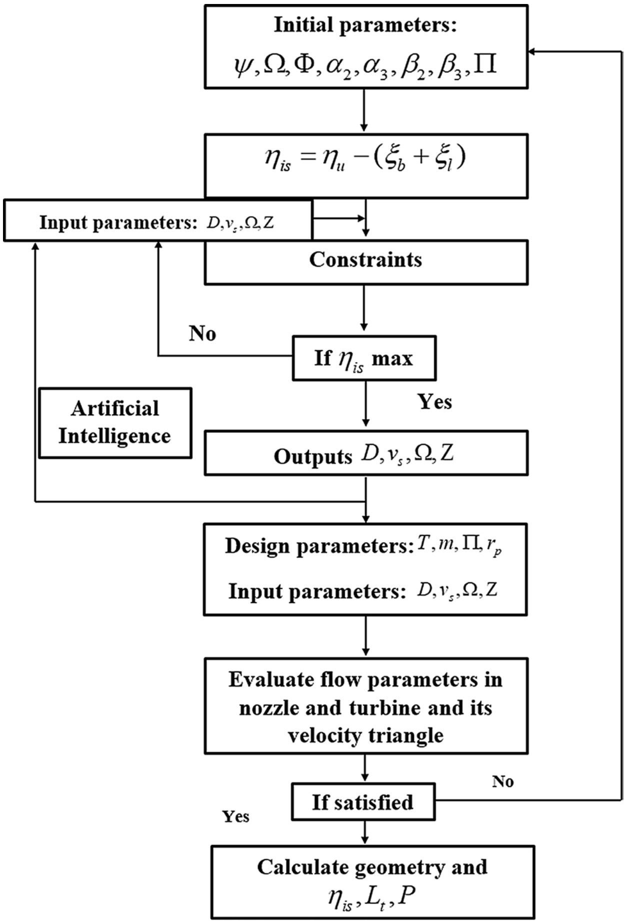

Fig. 2 Mean-line design approach of a radial inflow turbine

2.3 Sensitivity analysis of non-dimensional and geometrical variables

It is noted that the isentropic efficiency, total losses, and power output of the turbine are significantly affected by velocity ratio (v_s), degree of reaction (Ω), nozzle velocity coefficient (ϕ), turbine velocity coefficient (ψ), turbine diameter ratio (D), velocity ratio $\left(v_s\right)$, absolute inlet flow angle $\left(\alpha_1\right)$, and relative outlet velocity angle $\left(\beta_2\right)$. The velocity components are important to encounter the flow losses. It depends on different parameters like wall friction, boundary layer separation, secondary flow, etc. Since the flow field inside the turbine is complex due to the rotation, the turbine velocity coefficient (ψ)is usually less than the nozzle velocity coefficient (ϕ). The decrease in α_1 increases the turbine efficiency but at the same time, the nozzle losses may be increased; therefore, it is limited in a selected range as mentioned in Table 3. The decrease in β_2 reduces the turbine outlet velocity losses but it is limited by the manufacturing constraint.

The velocity ratio directly affects the efficiency of the turbine. The turbine diameter ratio is also an important parameter to define. The increase in diameter ratio increases the isentropic efficiency and reduces the total loss of the turbine. It is also useful in determining the outlet diameter of the turbine which is directly related to the impeller loss. The number of blades is a fundamental parameter on which the turbine losses and its efficiency depend. The less number of blades is always beneficial for flow stability, but the power output is low, whereas flow blockage and total losses are increased by increasing the number of blades. The inertia of the small turbine is also considered. In this regard, Glassman proposes a formula to determine the number of blades of the turbine which is as follows:

$$Z = \frac{\pi}{30}(110 - \alpha)\tan\alpha \tag{4}$$

where $\alpha = 90 - \alpha_2$.

2.3.1 Sobol method

The performance of radial turbine depends on the non-dimensional and geometrical design variables. It is complicated to identify the effect of these variables. Through the sensitivity analysis, the dependability of such variables on the performance of radial turbine can be evaluated. Sobol sensitivity analysis is a variance decomposition-based global sensitivity analysis method commonly used for nonlinear systems [35, 36]. In this study, Sobol method is utilized to evaluate the effectiveness of such design variables on the isentropic efficiency of the turbine.

The variance decomposition and the total output variance to input constants are derived as follows:

Fig. 3 **a** Schematic of the velocity triangle of the turbine, **b** turbine geometry

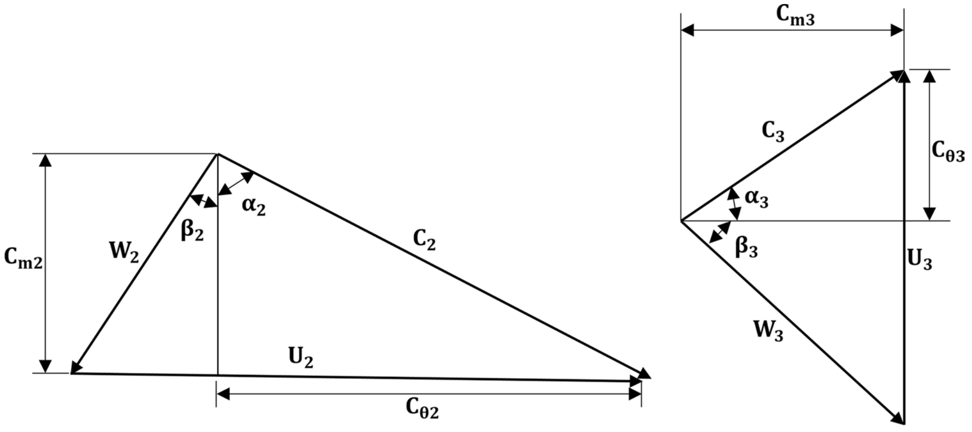

(a) Inlet and outlet velocity triangle of the turbine

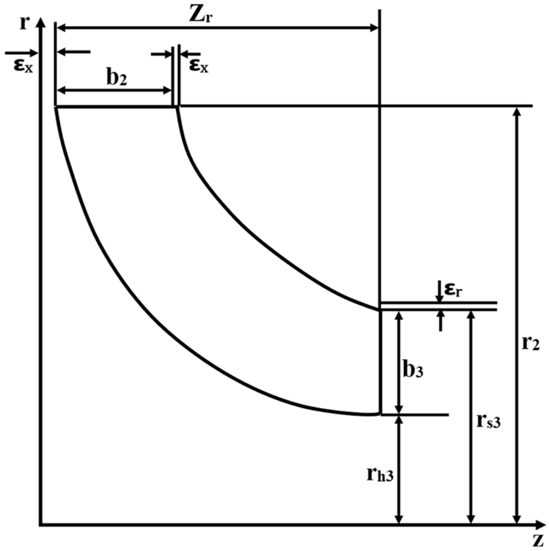

(b) The turbine geometry

$$\mathrm{Var}(Y) = \sum D_i(Y) + \sum D_{ij}(Y) + \cdots + D_{12\ldots d}(Y) \tag{5}$$

where $\mathrm{Var}(Y)$ is the total variance of total loss (output), $D_i(Y)$ is the first-order variance of input constants X_i and $D_{ij}(Y)$ is the second-order variance of X_i and X_j which are formulated as:

$$\mathrm{Var}(Y) = E(Y_i^2) - E^2(Y_i) \tag{6}$$

$$D_i(Y) = \mathrm{Var}\left[E(Y \mid X_i)\right] \tag{7}$$

Thus, the first-order sensitivity index is written as follows:

$$S_i = \frac{D_i(Y)}{\mathrm{Var}(Y)} \tag{8}$$

Figure 4 represents the sensitivity index of six non-dimensional variables. It is found out that the variation of isentropic efficiency is higher for D, v_s, Ω, and Z as compared to ϕ and ψ. The ranges of these design parameters used in this study are mentioned in Table 3.

Therefore, the isentropic efficiency, total losses, and power output are defined in the functional form as follows:

$$\eta_{\mathrm{is}} = f\left(v_{\mathrm{s}}, \Omega, D, Z\right) \tag{9}$$

$$L_{\mathrm{t}} = f\left(v_{\mathrm{s}}, \Omega, D, Z\right) \tag{10}$$

$$P = f\left(v_{\mathrm{s}}, \Omega, D, Z\right) \tag{11}$$

2.4 Design of nozzle

The flow at the outlet of the nozzle does not follow the blade profile path. It turns toward the meridional direction due to the boundary layer growth (accelerating flow) and instantaneous expansion because of trailing edge thickness. The

Table 3 Range of radial turbine performance parameters

Parameter	Range
v_s	0.62–0.74
Ω	0.36–0.50
Z	8–17
D	0.25–0.55
ϕ	0.88–0.98
α_1	11°–32°
β_2	28°–44°
ψ	0.70–0.92

Bold symbols indicates the most effective parameters

velocity at the exit of the throat consists of two components, C_{mt} and $C_{\theta t}$. The meridian component is perpendicular to the nozzle throat circle diameter, which determines the mass flow rate, whereas the other component $C_{\theta t}$ is tangential to the throat. Therefore, the meridional velocity component is used in defining the mass balance equation of a convergent-type nozzle which is as follows:

$$C_{\mathrm{mt}} = \frac{m}{\pi D_{\mathrm{t}} \rho_{\mathrm{t}} b_{\mathrm{t}}} \tag{12}$$

$$C_{\theta t} = \frac{C_0 D_2}{D_{\mathrm{t}}} \tag{13}$$

$$b_{\mathrm{t}} = 0.8 \times b_2 \tag{14}$$

$$D_{\mathrm{t}} = 1.068 \times D_2 \tag{15}$$

where D_{t}, C_{mt} and b_{t} are throat circle diameter, meridian component velocity, and height of the nozzle, respectively. Generally, it is lesser than turbine inlet blade height which enables small margin for expansion in annular space and also accommodating the axial misalignment.

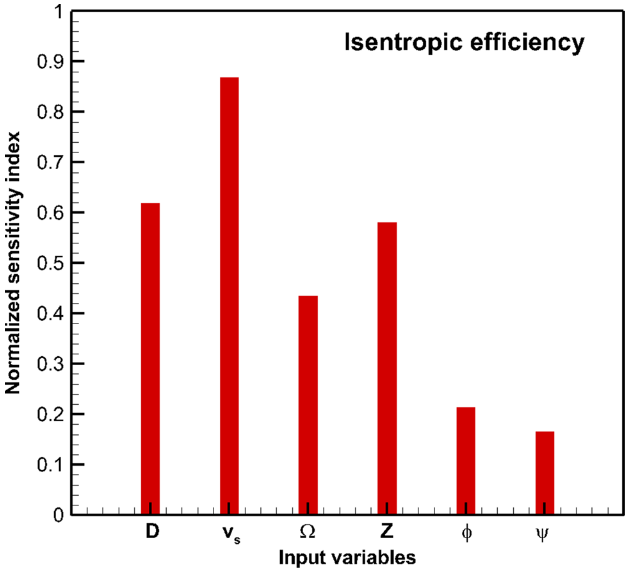

Fig. 4 Sensitivity analysis of isentropic efficiency

2.5 Sizing of the nozzle vanes

The throat angle for the trailing edge thickness of the nozzle is calculated using conservation of momentum and continuity of the flows. Aerodynamically, it is preferable to make the trailing edge finer under mechanical design limit. The throat width (W_{t}) and the throat angle (α_{t}) are calculated based on continuity equation:

$$W_{\mathrm{t}} = \frac{m_{\mathrm{t}}}{Z_{\mathrm{n}} \rho_{\mathrm{t}} b_{\mathrm{t}} C_{\mathrm{t}}} \tag{16}$$

$$\alpha_{\mathrm{t}} = \tan^{-1}\left(\frac{C_{\mathrm{mt}}}{C_{\theta t}}\right) \tag{17}$$

The nozzle throat outlet angle must be different from the turbine blade inlet angle. This inconsistency is permitted for the expansion of the fluid in the vaneless space.

The losses inside the nozzle are directly related to its number of blades. The increase in the number of blades can guide the flow in a better way, but at the same time, it induces the frictional losses. Generally, the prime number is used for the number of blades in the nozzle. The blade pitch length (p_{n}), nozzle ring inner diameter (D_{n}), and chord length $(\mathrm{Ch}_{\mathrm{n}})$ are calculated as:

$$P_{\mathrm{n}} = \frac{\pi D_{\mathrm{t}}}{Z_{\mathrm{n}}} \tag{18}$$

$$D_{\mathrm{n}} = \sqrt{D_{\mathrm{t}}^2 + W_{\mathrm{t}}^2 - 2W_{\mathrm{t}} D_{\mathrm{t}} Cos\left(\alpha_{\mathrm{t}}\right)} \tag{19}$$

$$Ch_{\mathrm{n}} = \frac{2s\left(\cot\alpha_{\mathrm{t}} - \cot\alpha_0\right)\sin^2\alpha_{\mathrm{t}}}{\psi_z \sin\lambda} \tag{20}$$

The solidity value is obtained from the aerodynamic load coefficient ψ_z, which may be defined as the ratio of actual tangential force to ideal tangential force, renowned as Zweifel number. The optimal value for the aerodynamic load coefficient is taken to be 0.82.

3 ANN and ANFIS models

The ANN and ANFIS are soft computing models which are developed using the design variable of a radial inflow turbine to predict their ranges in which it has the highest performance. The models are developed to predict the isentropic efficiency, total losses, and power output of a radial inflow turbine with a set of design variables using MATLAB® 17.*b* toolbox.

3.1 ANN model development

The number of layers, neurons, and transfer function type are identified in the ANN model. The multilayer perceptron (MLP) neural network with a single hidden layer has opted for the training process using a backpropagation algorithm. Three transfer functions (TFs) are used for a comparative study of data prediction in hidden as well as the output layer. From several trials, the best network is obtained and the hidden neurons variation in the range of 1–10. For every hidden neuron, the training process is repeated. The details of the ANN model are mentioned in Table 4.

The ANN model is developed using the aforementioned four non-dimensional inputs variable for the prediction of the isentropic efficiency, total losses, and power output. Initially, the datasets are divided into three parts, namely training, testing, and validation datasets containing 80%, 10%, and 10% , respectively. The training data train the network, and the accuracy of the network is tested by the validation datasets. Figure 5 represents a schematic of an MLP with a single hidden layer. Every unit in the network is connected with the node in the very next layer. The input parameters are given to the network; it can multiply with the weight of the hidden neurons. The weighted input values are summed up and transformed when it passes through the hidden neurons. The output of the hidden layer is the input of the next layer, and the process is continued in the forward direction. The functional relation is expressed as follows:

$$y_m = g\left(\sum_{j=0}^{k} w_{mj}^{2}\varphi\left(\sum_{i=0}^{n} w_{ji}^{1}x_i\right)\right) \tag{21}$$

where n is the inputs, k is the hidden neurons, and m is the outputs.

Table 4 Details of ANN model

Parameter	Value
Number of inputs	4
Number of outputs	3
Network structure	MLP
Number of hidden layers	1
Training algorithm	Backpropagation
Transfer function	Logsig, Purelin, Tansig
Error function	MSE
Number of epochs	1000
Hidden neuron range	1−10 with step size one

3.2 ANFIS model development

The fuzzy system is a computing framework originated from fuzzy set theory, if-then rules, and fuzzy reasoning. When the system combines with the neural network, it advantages the assimilating features of the neural network and has an implementation equal to the fuzzy inference model [37]. ANFIS model is developed to estimate the isentropic efficiency, total losses, and power output of the turbine with a set of design variables. There are four input and three output variables which are divided into 80% and 20% datasets for training and validation purpose.

3.3 Structure of adaptive neuro-fuzzy inference system

The number of input membership functions (MFs) is determined to establish an ANFIS network. MFs are arbitrary curves which depend on the type of application that can be utilized. Theoretically, the increase in MFs can decrease the error until it reaches its minimum value; after that further increase in MFs deduces less error but takes higher computational time. Therefore, to determine the optimum number of MFs, the error occurred from each network is checked by varying the number of MFs until the errors stop to decrease and that MFs is the optimum one. In the present case, four MFs for every input are opted [38]. There are various membership functions types available; but for the present case, Gauss, Tri, Trap, and Gbell MFs are employed for input parameters and compared their predicted results, training, and testing errors. For the output parameters, a linear MF has opted. The basic structural information of ANFIS network is shown in Fig. 6 and Table 5.

Fig. 5 Schematic of the ANN model network

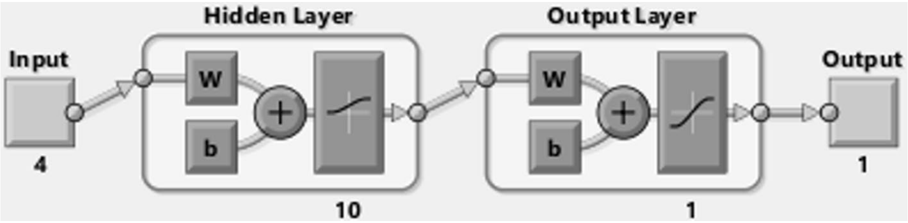

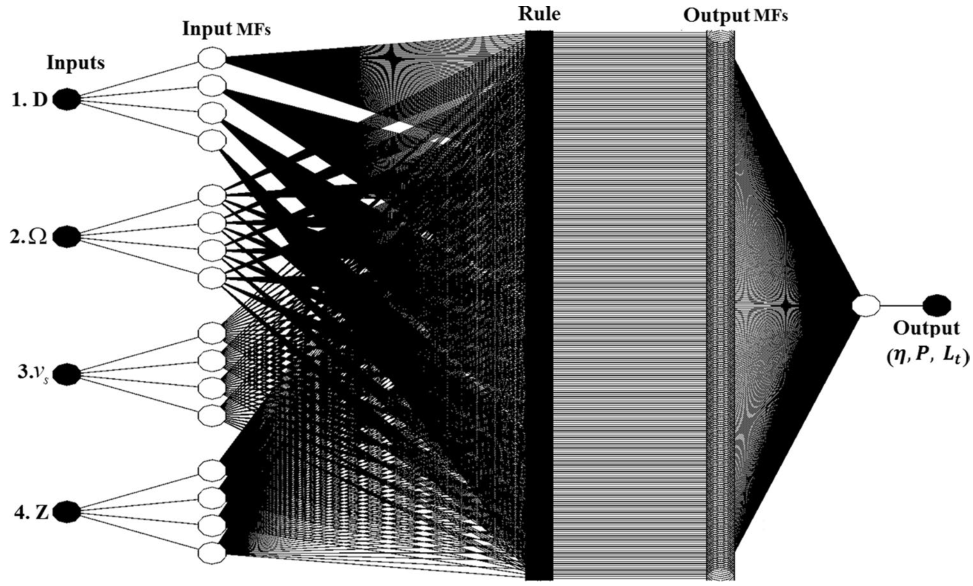

Fig. 6 Basic structure of ANFIS

Table 5 ANFIS network design

MFs type of input parameters	Gauss, Tri, Trap, Gbell
MF type of output parameters	Linear
Number of MFs	4
Optimization method	Hybrid
Number of training data	54
Number of epochs	200

The output of first-order T–S FIS with IF–THEN fuzzy inference rules are expressed as follows:

- Rule-1: If $x = A_i$ and $y = B_j$ then

$$f_i = p_i x_1 + q_i y_n + r_i \tag{22}$$

where x and y are non-fuzzy inputs variables, f_i is the output in the fuzzy region which is specified by the fuzzy rules, A_i and B_j are fuzzy variables of the MFs, p_i, q_i, and r_i are design parameters (first-order polynomial) which are determined in the training process.

The performance of the model is verified using three error factors including R-squared, mean absolute error MAE, and root-mean squared Error (RMSE) which are as follows:

$$R^2 = 1 - \frac{\Sigma_{t=1}^{N}\left(f_t - O_t\right)^2}{\Sigma_{t=1}^{N}\left(f_t - \bar{f}_t\right)^2} \tag{23}$$

$$\mathrm{MAE} = \frac{1}{N} \times \Sigma_{t=1}^{N} \mid f_t - O_t \mid \tag{24}$$

$$\mathrm{RMSE} = \sqrt{\frac{1}{N} \times \Sigma_{t=1}^{N}\left(f_t - O_t\right)^2} \tag{25}$$

where O_t is model output, f_t is overall output, N is the total number of samples, and t is the number of samples.

ANFIS structure contains five layers of neurons. Each neuron performs as a processing element with the activation function to generate the output [37].

3.4 ANN and ANFIS results

Table 6b shows that the LOGSIG transfer function is best fitted for this ANN network because of minimum error. Figure 7 illustrates the comparison of regression curves of calculated and predicted isentropic efficiency, total losses and power output for LOGSIG transfer function.

Initially, the ANFIS networks are trained based on the non-dimensional variables used in the designing process. There are three networks: ANFIS-1 estimates the isentropic efficiency, ANFIS-2 estimates the total losses, and ANFIS-3 estimates the power output. Table 6c shows a comparison of the predicted results from four different types MFs (Gauss, Tri, Trap, and Gbell), out of which the training and testing error of Gauss MF has less. Therefore, decision surfaces obtained from Gauss MF are presented hereafter. The final decision surfaces obtained from ANFIS training are represented in Figs. 8, 9 and 10. It illustrates that the isentropic efficiency of the turbine is higher when Ω and Z is in the range of 0.42−0.48 and 10−14 , whereas the diameter ratio (D), and v_s in the range of 0.35−0.50 and 0.67−0.70 , respectively. In this range, the power output is on the higher side which is directly related to the refrigerating capacity of the system. But the total losses are also on the higher side in

Table 6 Comparison of variation of output parameters with different geometrical inputs of helium turbine and its prediction by ANN and ANFIS methods

(a) Geometrical input and output parameters

Geometrical input parameters				Output parameters		
D	v_s	Ω	Z	η_s	L_t	$P(kW)$
0.26	0.66	0.48	11	0.802	0.136	6.83
0.28	0.72	0.49	10	0.696	0.335	3.61
0.36	0.71	0.44	15	0.721	0.281	3.74
0.48	0.64	0.41	8	0.729	0.134	6.24
0.52	0.66	0.39	12	0.764	0.227	7.68
0.38	0.67	0.46	12	0.826	0.316	7.95
0.42	0.69	0.48	11	0.742	0.207	6.11
0.39	0.72	0.41	13	0.794	0.286	6.95
0.45	0.71	0.45	11	0.815	0.293	8.14
0.44	0.63	0.38	9	0.671	0.116	4.51

(b) Predicted ANN results for different transfer functions

ANN results

Logsig			Purelin			Transig		
η	L_t	P	η	L_t	P	η	L_t	P
0.801	0.134	6.79	0.798	0.132	6.81	0.796	0.139	6.78
0.694	0.331	3.58	0.664	0.338	3.65	0.681	0.341	3.54
0.711	0.276	3.71	0.712	0.289	3.74	0.711	0.288	3.64
0.730	0.128	6.31	0.731	0.131	6.34	0.726	0.134	6.38
0.761	0.224	7.59	0.759	0.229	7.54	0.751	0.229	7.51
0.831	0.309	7.98	0.832	0.289	7.89	0.829	0.326	8.01
0.741	0.199	6.15	0.737	0.195	6.11	0.738	0.214	6.18
0.796	0.274	6.98	0.782	0.281	6.94	0.796	0.291	6.88
0.812	0.281	8.26	0.801	0.299	8.11	0.814	0.297	8.17
0.669	0.117	4.49	0.675	0.121	4.50	0.669	0.119	4.51

(c) Estimated ANFIS results for different MFs

Gauss			Tri			Trap			Gbell		
η	L_t	P	η	L_t	P	η	L_t	P	η	L_t	P
0.801	0.135	6.82	0.796	0.138	6.79	0.791	0.137	6.91	0.786	0.133	6.61
0.694	0.338	3.63	0.701	0.331	3.65	0.681	0.332	3.66	0.684	0.337	3.69
0.718	0.279	3.71	0.711	0.284	3.69	0.716	0.282	3.70	0.732	0.284	3.88
0.730	0.134	6.28	0.718	0.136	6.19	0.715	0.136	6.29	0.711	0.133	6.30
0.766	0.228	7.69	0.746	0.231	7.73	0.759	0.232	7.63	0.752	0.228	7.59

Table 6 (continued)

(c) Estimated ANFIS results for different MFs

	Gauss			Tri			Trap			Gbell		
	η	L_t	P	η	L_t	P	η	L_t	P	η	L_t	P
	0.819	0.318	7.94	0.814	0.324	7.91	0.819	0.325	7.84	0.809	0.311	8.01
	0.738	0.209	6.12	0.731	0.214	6.05	0.738	0.216	6.21	0.761	0.199	6.23
	0.789	0.284	6.98	0.786	0.289	6.89	0.785	0.290	6.79	0.785	0.291	6.99
	0.809	0.295	8.11	0.786	0.298	7.98	0.801	0.301	8.33	0.837	0.298	8.21
	0.664	0.117	4.52	0.662	0.119	4.49	0.674	0.121	4.61	0.651	0.114	4.46
Training errors$(\times 10^{-3})$	0.193	0.012	0.431	0.230	0.019	0.80	0.196	0.020	0.619	0.198	0.022	0.793
Testing errors	0.736	0.721	0.694	0.954	0.793	0.968	0.872	0.737	0.741	0.894	0.743	0.866

these zones. Therefore, we have to compromise between the isentropic efficiency, power output, and total losses. The samples of geometrical input and output parameters and its predicted values from ANN and ANFIS are summarized in Table 6. Based on the predicted geometrical variables, the major geometrical specifications of the turbine and nozzle are mentioned in Table 7.

4 Numerical methodology

4.1 Computational domain and mesh generation

The numerical analysis is limited to the turbine and nozzle, which are the critical components on which the performance of the system depends. The obtained dimensions of the turbine and nozzle from the one-dimensional design are transferred to ANSYS BladeGen in which three-dimensional models are generated. The computational domain represents a single blade passage, and is discretized using a multi-block structured grid which is generated using ANSYS Turbo-Grid. The *H*-type topology is used for inlet and outlet blocks, whereas *J*/*O* type is selected for the passage block to solve the near-wall region which is required for boundary layer flow visualization near the wall. The node distribution of the grid and its scheme are mentioned in Table 8. The *O*-grid includes in the periodic boundary and from hub to shroud in the passage block. Since the mesh in the nozzle and turbine are generated separately, the GGI connection has opted for combining the interface mesh in ANSYS CFX. Apart from this, the $y+$ value which shows the non-dimensional distance from the wall is also considered to solve the boundary layer effect in the vicinity of the turbine blade and flow passages. The opted $y+$ value for all the models is mentioned in Table 9.

4.2 Boundary conditions

The total pressure (16, 8, and 4.5 bar) and total temperature (80, 60, and 48 K) are set at the nozzle inlet and the static pressure (8, 4.5, and 2 bar) has opted at the turbine outlet. The walls (hub, blade, and shroud) are assumed to be adiabatic and hydraulically smooth. It is also assumed that the fluid velocity is negligible relative to the solid wall boundary. For this reason, non-slip boundary condition is imposed on the walls. The rotational speed of high-, medium-, and low-pressure turboexpander is set to be 0.24, 0.19, and 0.15 million, respectively. Additionally, the numerical analysis is performed using a single blade flow passage in place of simulating the whole turboexpander. In this regard, the rotational periodicity is applied along the circumferential direction of the flow passage to reduce the computational overhead. Figure 11 illustrates the details of the computational domain.

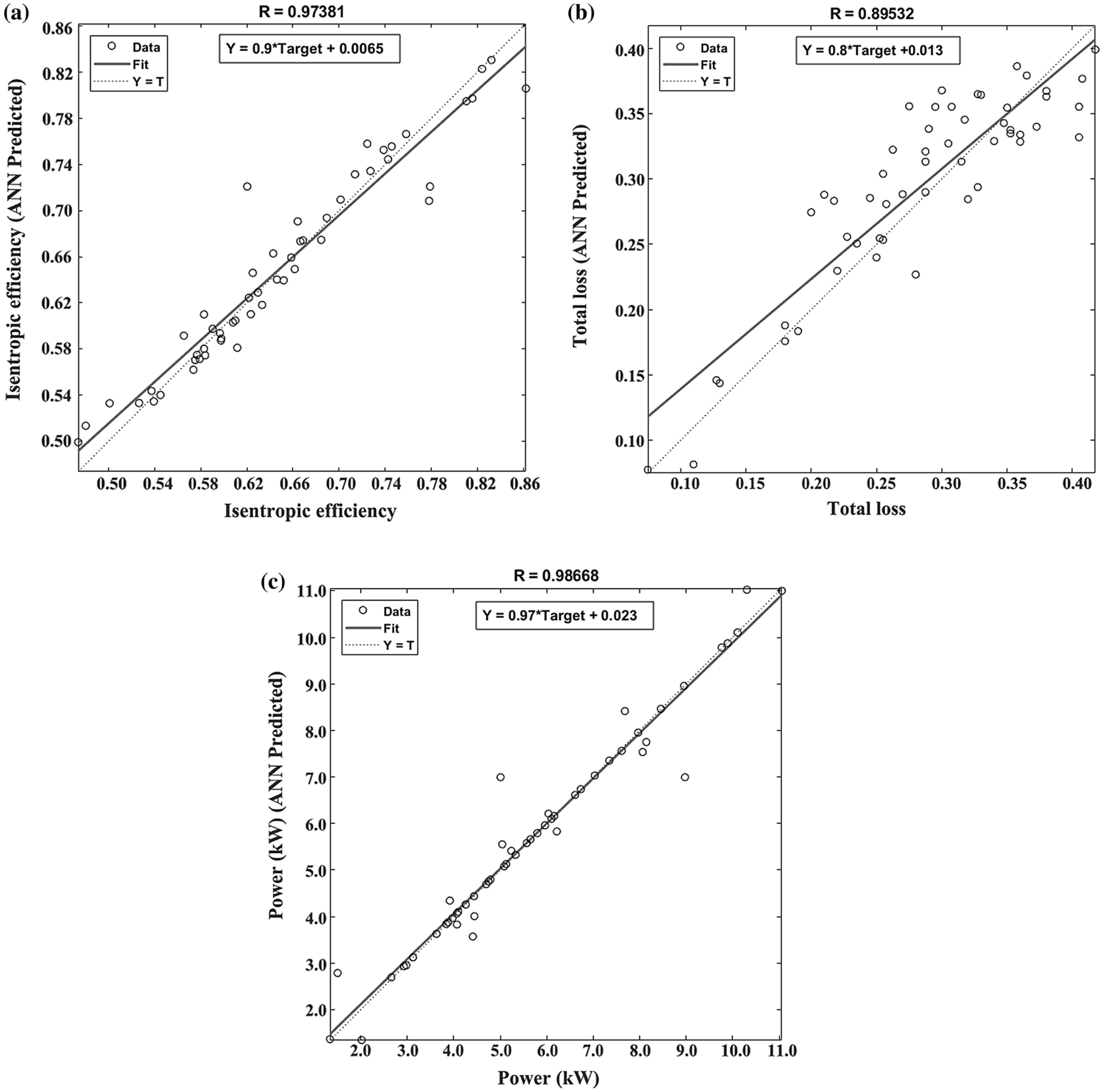

Fig. 7 Regression curve of ANN **a** isentropic efficiency, **b** total losses (L_t), **c** power output

4.3 Numerical setup

Firstly, the interface between the nozzle and turbine is modeled as a stage frame change (mixing plane) with automatic pitch change to compute the rotation of turbine in steady-state condition. In this method, the fluid around the blade is set as a moving reference frame, whereas the blade and hub are assumed to be stationary with respect to the inner fluid. In this way, there is no need for grid movement during the steady-state simulation. Secondly, a sliding mesh method has opted during transient blade row simulation with automatic pitch change. The flow through the turbine is analyzed in a rotating coordinate system to consider the rotational effect. Therefore, the transient rotor–stator model is imposed at the interface of the two domains. The rotor domain rotates at each time step which is defined by the pitch ratio. Thus, the boundary nodes of nozzle and turbine domain slide with respect to each other. Transient simulations are run using the passing period and second-order backward Euler transient scheme. The maximum number of loops is fixed to be 10.

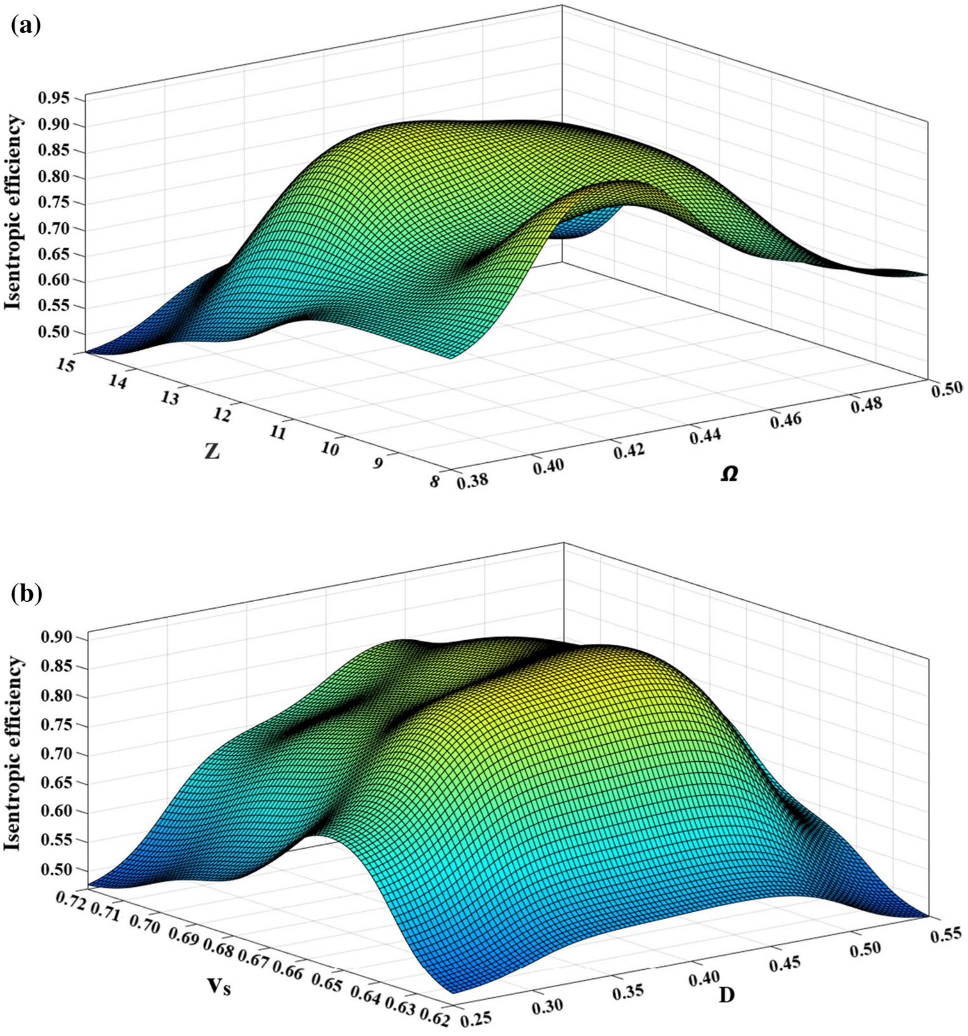

Fig. 8 Decision surface of isentropic efficiency **a** degree of reaction (Ω) and number of blade (Z), **b** velocity ratio $\left(v_s\right)$ and diameter ratio (D)

The turbulence intensity is set to be 5%. The convergence and conservation criteria are set when normalized residuals are less than 10^{-6} and 10^{-5} , respectively. The simulation takes about 150 h to obtain a converged solution on Intel®Xeon®CPU E5-1660 v3 @ 3.00 GHz with 64 GB RAM system.

4.4 Turbulence model and governing equations

Reynolds-averaged Navier–Stokes (RANS) equation with finite volume solver is used for numerical simulations using commercial CFD platform ANSYS CFX. Navier–Stokes equations are discretized using a second-order upwind advection scheme. The better visualization of the near-wall flow among the available turbulence models, $k-\omega$ shear stress turbulence (SST) model is used to conduct the transient blade row analysis for flow visualization taken effect of gravity into the count [39]. The $k-\epsilon$ turbulence model can enumerate the eddy viscosity in the RANS by resolving turbulent kinetic energy and turbulent dissipation rate. Although, the model is computationally stable but cannot estimate the secondary flow behavior, flow separation, and reattachment point accurately. The $k-\omega$ SST model possesses assimilating features of $k-\omega$ and $k-\epsilon$ model. The inner portion of boundary layer is solved by $k-\omega$ turbulence model, whereas the wake region and free shear layers are considered by $k-\epsilon$ model. A blending function is defined for even transformation between the two models. This model is used due to its better capability for automatic wall treatment of the nodes near the wall to capture the turbulence closure and flow separation [40]. The shear stress transport (SST) $k-\omega$ turbulence model has opted for its capability to capture the turbulence closure and flow separation effects on the eddy viscosity. This turbulence model can accurately predict the turbomachinery flows having boundary layer separations [41, 42]. In this aspect, the $k-\omega$ SST model can predict the boundary layer through the passage (excellent turbulent boundary layer modeling behavior), in which ω near the wall is more stable than that of the ϵ. The governing

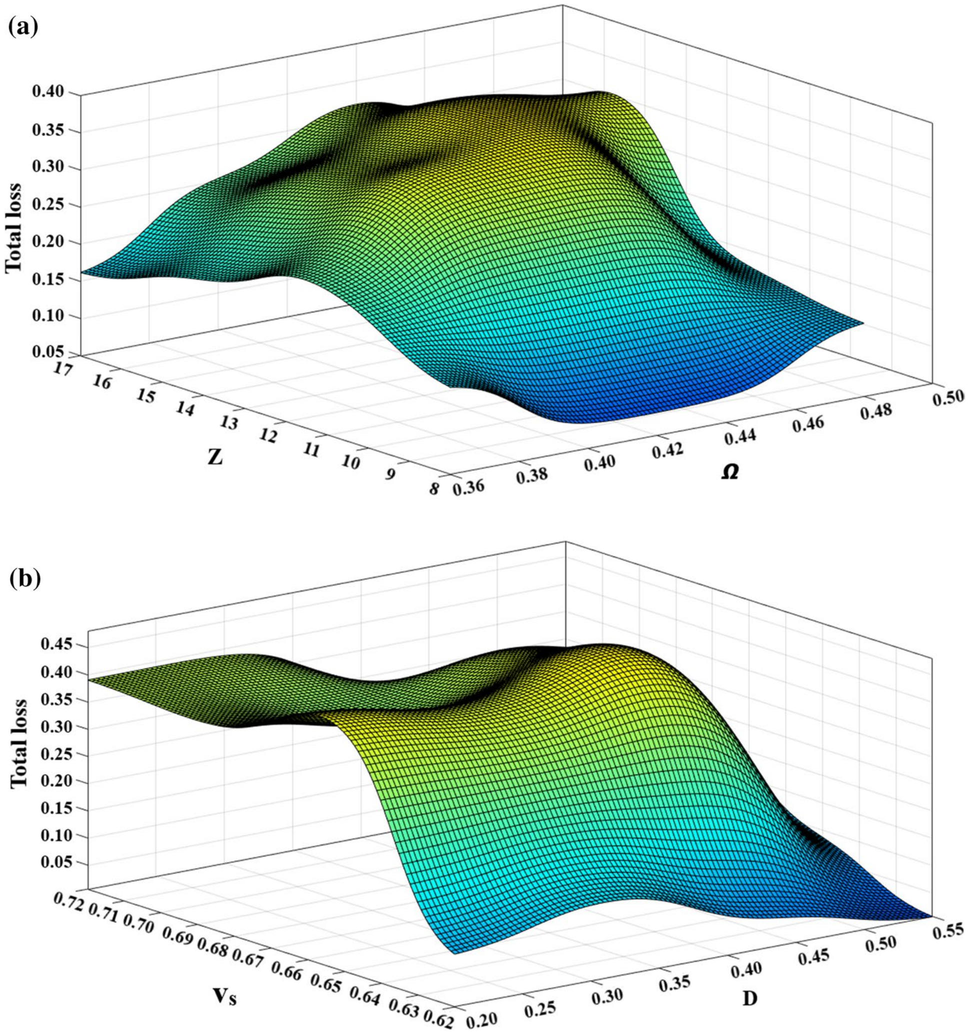

Fig. 9 Decision surface of total losses **a** degree of reaction (Ω) and number of blade (Z), **b** velocity ratio $\left(v_s\right)$ and diameter ratio (D)

equations used in the numerical simulations are mentioned as follows:

4.4.1 Continuity equation

$$\frac{\partial \rho}{\partial t} + \frac{\partial}{\partial x_j}\left(\rho U_j\right) = 0 \tag{26}$$

4.4.2 Momentum equation

Since the analysis has been done in rotating coordinate frame, the conservation of momentum equation in terms of velocity components (radial, tangential) U_r, U_θ , and U_z are written as [43]:

$$\begin{aligned} &\frac{\partial}{\partial t}\left(\rho U_r\right) + \frac{1}{r}\frac{\partial}{\partial r}\left(\rho r U_r U_r\right) + \frac{1}{r}\frac{\partial}{\partial \theta}\left(\rho U_r U_\theta\right) \\ &\quad + \frac{\partial}{\partial z}\left(\rho U_r U_z\right) - \frac{\rho U_\theta^2}{r} - 2\rho\Omega U_\theta \\ &\quad - \rho\Omega^2 r = -\frac{\partial p}{\partial r} + F_r \end{aligned} \tag{27}$$

$$\begin{aligned} &\frac{\partial}{\partial t}\left(\rho U_\theta\right) + \frac{1}{r}\frac{\partial}{\partial r}\left(\rho r U_r U_\theta\right) + \frac{1}{r}\frac{\partial}{\partial \theta}\left(\rho U_\theta U_\theta\right) \\ &\quad + \frac{\partial}{\partial z}\left(\rho U_r U_\theta\right) + 2\rho\Omega U_r = -\frac{\partial p}{r\partial \theta} + F_\theta \end{aligned} \tag{28}$$

$$\begin{aligned} &\frac{\partial}{\partial t}\left(\rho U_z\right) + \frac{1}{r}\frac{\partial}{\partial r}\left(\rho r U_r U_z\right) + \frac{1}{r}\frac{\partial}{\partial \theta}\left(\rho U_z U_\theta\right) \\ &\quad + \frac{\partial}{\partial z}\left(\rho U_z U_z\right) = -\frac{\partial p}{\partial z} + F_z \end{aligned} \tag{29}$$

4.4.3 Total energy equation

$$\frac{\partial\left(\rho h_{tot}\right)}{\partial t} - \frac{\partial p}{\partial t} + \nabla.\left(\rho U h_{tot}\right) = \nabla.(\lambda \nabla T) + \nabla.(U.\tau) + U.S_M + S_E \tag{30}$$

where S_E is the source term (energy), τ is the mean stress tensor, and h_{tot} is the total enthalpy:

$$\tau = \mu\left(\nabla U + (\nabla U)^T - \frac{2}{3}\delta\nabla.U\right) \tag{31}$$

Fig. 10 Decision surface of power output **a** degree of reaction (Ω) and number of blade (Z), **b** velocity ratio $\left(v_s\right)$ and diameter ratio (D)

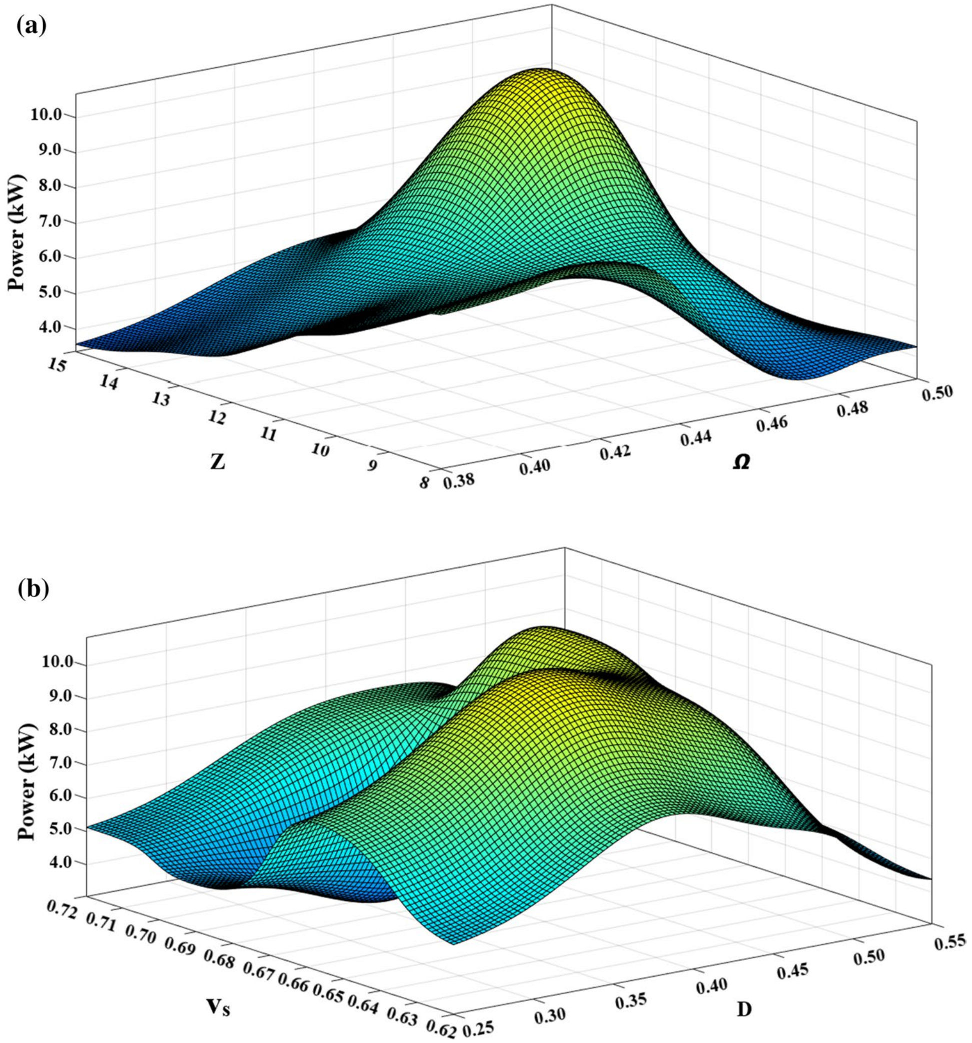

Table 7 Major geometrical specifications of the turbine and nozzle

Specifications	Model 1	Model 2	Model 3
Turbine diameter (mm)	15.74	16.08	16.22
Turbine inlet blade height (mm)	0.65	0.67	0.68
Turbine outlet blade height (mm)	2.65	2.68	2.49
Turbine hub diameter (mm)	5.21	5.24	5.25
Shroud clearance (mm)	0.1	0.1	0.1
Number of nozzle blades	17	19	21
Number of turbine blades	10	11	13
Tip clearance (mm)	0.1	0.1	0.1

$$h_{tot} = h + \frac{1}{2}U^2 \tag{32}$$

For the rotating frame of reference, to observe the effects of Coriolis and centrifugal forces, additional sources of momentum have been taken into account at constant angular velocity ω.

$$S_{\mathrm{M,rot}} = S_{\mathrm{Cor}} + S_{\mathrm{cfg}} \tag{33}$$

$$S_{\mathrm{Cor}} = -2\rho\omega \times U \tag{34}$$

$$S_{\mathrm{cfg}} = -\rho\omega \times (\omega \times r) \tag{35}$$

Table 8 Node distribution and its scheme in different blocks (models 1/2/3)

(Model 1/2/3)	Inlet block		Outlet block		Passage block	
	Streamwise	Blade-to-blade	Streamwise	Blade-to-blade	Streamwise	Blade-to-blade
Turbine	22/20/20	54/52/50	20/20/18	36/34/34	86/86/82	40/40/38
Nozzle	16/16/16	35/36/36	14/14/14	34/32/34	54/54 /50	28/28/28

Table 9 Non-dimensional wall distance of the turbine and nozzle (model 1/2/3)

Sections (Model 1/2/3)	$y+$ value	Sections (Model 1/2/3)	$y+$ value
Turbine inlet	0.8/0.8/0.8	Nozzle inlet	0.92/0.90/0.90
Near turbine blade	0.72/0.72/0.72	Near nozzle blade	0.85/0.85/0.86
Center of the flow passage	1.4/1.4/1.6	Center of the flow passage	1.8/2.0/2.0
Turbine outlet	0.86/0.86/0.86	Nozzle outlet	0.78/0.78/0.78

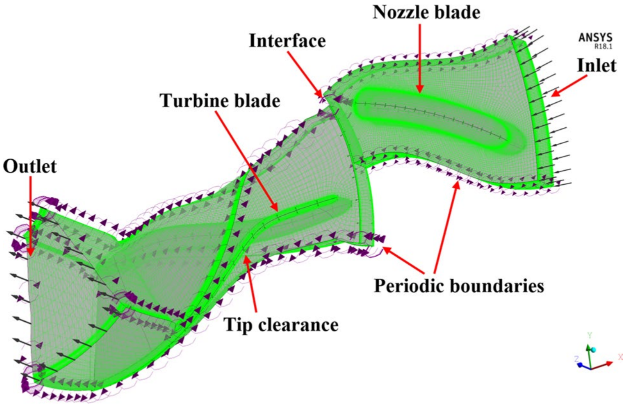

Fig. 11 Computational fluid domain and boundary setup for nozzle and turbine

where r and U are the location vector and relative frame velocity vector, respectively. Advection and transient scheme use rothalpy (I) in place of total enthalpy $\left(h_t\right)$ for energy equation (Eq. 5).

$$I = h_{stst} + \frac{1}{2}U^2 - \frac{1}{2}\omega^2 r^2 \tag{36}$$

The term $\nabla.(U.\tau)$ represents the work due to viscous stress, which is called as viscous work. Internal heating due to the viscosity of the fluid is assumed to be negligible. The term $U.S_M$ represents work due to external momentum which is neglected in this solution.

4.4.4 SST *k-ω* governing equations

4.4.5 Turbulence kinetic energy

$$\frac{\partial k}{\partial t} + U_j\frac{\partial k}{\partial x_j} = P_k - \beta^* k\omega + \frac{\partial}{\partial x_j}\left[\left(\nu + \sigma_k \nu_T\right)\frac{\partial k}{\partial x_j}\right] \tag{37}$$

4.4.6 Specific dissipation rate

$$\begin{aligned}\frac{\partial \omega}{\partial t} + U_j\frac{\partial \omega}{\partial x_j} &= \alpha S^2 - \beta\omega^2 + \frac{\partial}{\partial x_j}\left[\left(\nu + \sigma_\omega \nu_T\right)\frac{\partial \omega}{\partial x_j}\right] \\ &\quad + 2\left(1 - F_1\right)\sigma_{\omega 2}\frac{1}{\omega}\frac{\partial k}{\partial x_i}\frac{\partial \omega}{\partial x_i}\end{aligned} \tag{38}$$

where α, and β are constants and $F_1$is blending function.

$$F_1 = \tanh\left\{\left\{\min\left[\max\left(\frac{\sqrt{k}}{\beta^*\omega y}, \frac{500\nu}{y^2\omega}\right), \frac{4\sigma_{\omega^2}k}{CD_{k\omega}y^2}\right]\right\}^4\right\} \tag{39}$$

where $\beta^*$is a constant and $CD_{k\omega}$ is represented as:

$$CD_{k\omega} = \max\left(r\rho\sigma_{\omega^2}\frac{1}{\omega}\frac{\partial k}{\partial x_i}\frac{\partial \omega}{\partial x_i}, 10^{-10}\right) \tag{40}$$

ν_T is kinematic eddy viscosity represented as:

$$\nu_T = \frac{a_1 k}{\max\left(a_1\omega, SF_2\right)} \tag{41}$$

F_2 is the second blending function represented as:

$$F_2 = \tanh\left[\left[\max\left(\frac{2\sqrt{k}}{\beta^*\omega y}, \frac{500\nu}{y^2\omega}\right)\right]^2\right] \tag{42}$$

P_k is production limiter:

$$P_k = \min\left(\tau_{ij}\frac{\partial U_i}{\partial x_j}, 10\beta^* k\omega\right) \tag{43}$$

4.5 Real gas model

The implementation of the equation of state significantly affects the accuracy of the numerical results. In this regard, the Peng–Robinson real gas equation of state is used in the CFD simulations.

$$P = \frac{RT}{v - b} - \frac{a(T)}{v^2 + 2bv - b^2} \tag{44}$$

where a, a_0, b are constants which is find out as follows:

$$b = 0.0778\frac{RT_c}{P_c} \tag{45}$$

$$a(T) = a_0\left(1 + n\left(1 - \sqrt{\frac{T}{T_c}}\right)\right)^2 \tag{46}$$

$$a_0 = 0.45724\frac{R^2T_c^2}{P_c} \tag{47}$$

Table 10 Grid independence analysis (model 1/2/3)

Nozzle (nodes in million)	Turbine (nodes in million)	Isentropic efficiency	CPU time (h)
0.30/0.29/0.30	0.54/0.52/0.54	0.68/0.73/0.72	92/90/91
0.51/0.50/0.51	0.86/0.85/0.86	0.72/0.76/0.75	126/129/128
0.78/0.79/0.78	1.45/1.44/1.46	0.75/0.79/0.77	151/153/153
1.30/1.29/1.30	1.96/1.94/1.97	0.76/0.80/0.78	176/179/181

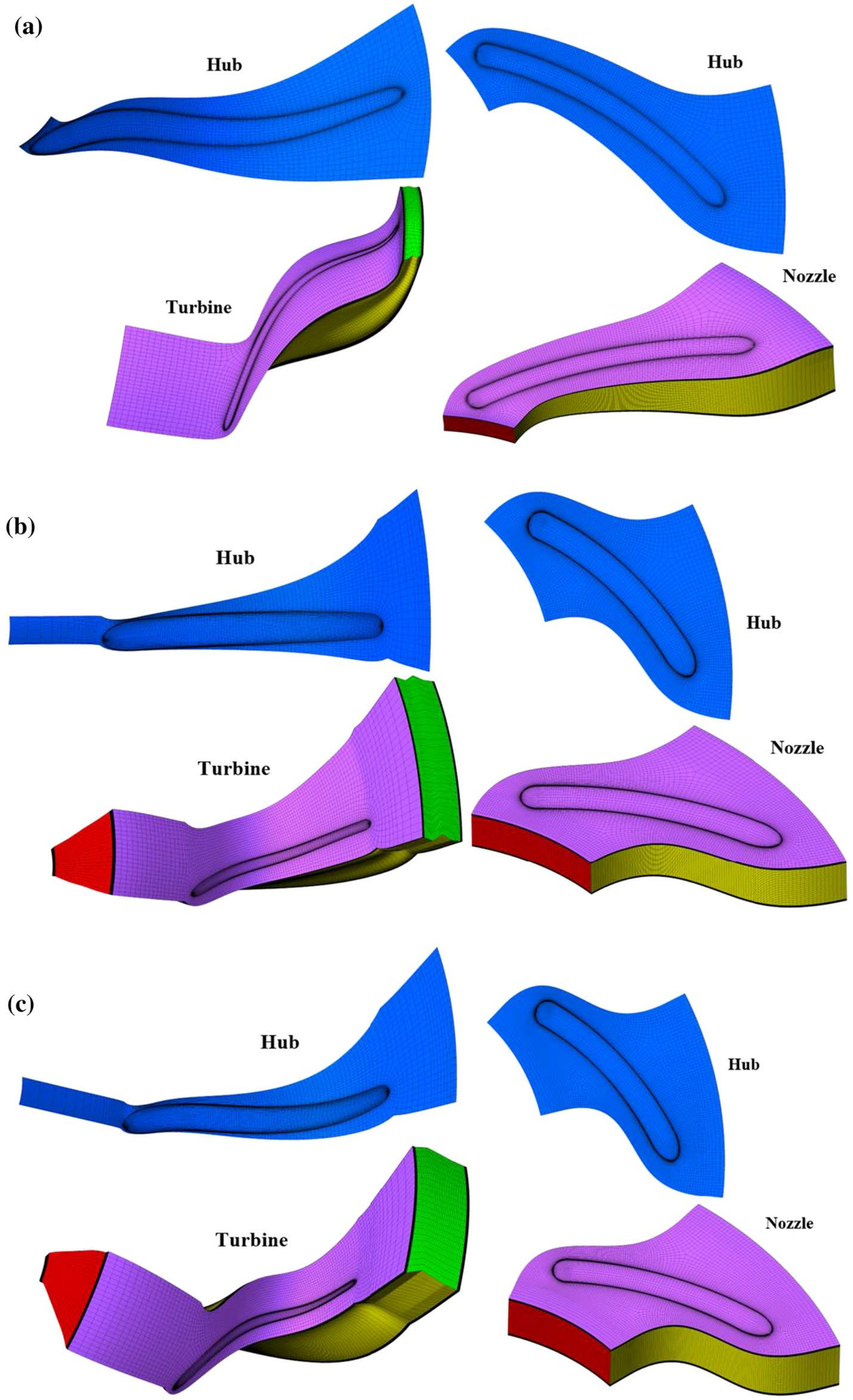

Fig. 12 Three-dimensional mesh of nozzle and turbine passages **a** model 1, **b** model 2, **c** model 3

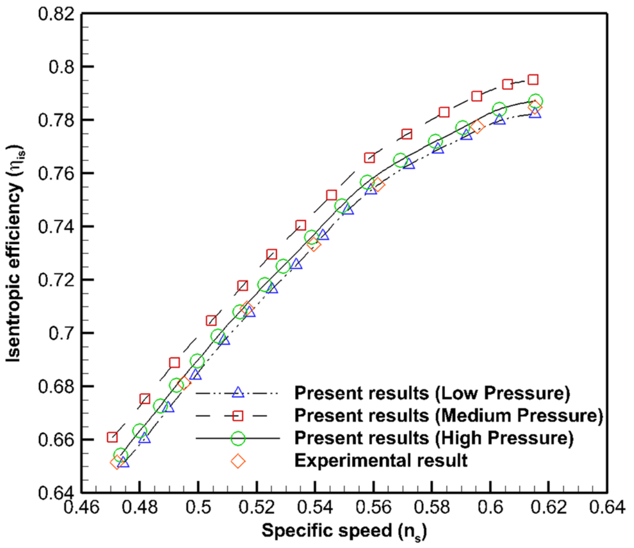

Fig. 13 Comparison of the present numerical results with experimental investigation [44]

and 'n' is calculated as follows:

$$n = 0.480 + 1.574\omega - 0.176\omega_0^2 \tag{48}$$

where 'ω' is the acentric factor.

4.6 Grid independence analysis

To examine the authenticity of the numerical results, a grid independence test is carried out. For this purpose, four grid resolutions for all the models are used to discretize the computational domain. The isentropic efficiency and computational time for obtaining a converged solution are compared which are mentioned in Table 10. It is observed that among the four investigated grid resolutions, the difference in the isentropic efficiency of the third and fourth rows is least. After that, the computational time is increased with less effect on the isentropic efficiency. Therefore, as a compromise between the accuracy of the results and computational time, the third row of Table 10 is opted for the remainder of the analysis. The three-dimensional images of the final mesh of nozzle and turbine flow passages are represented in Fig. 12.

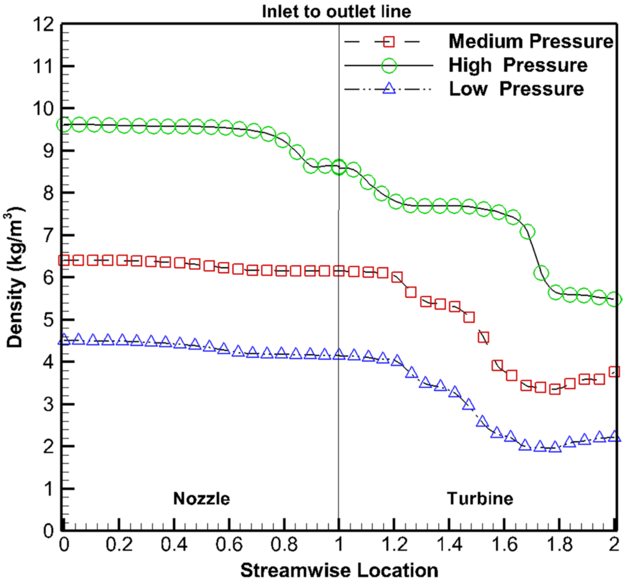

Fig. 14 Area-averaged density variation along the streamwise location

4.7 Assumptions at the rotor–stator interface

The stator and rotor connection is made for fully developed flow to overcome the pressure loss. The following assumptions are taken in the present numerical study:

- The total enthalpy is conserved in between the stator outlet and the rotor inlet, as this zone is considered as an adiabatic, and there is no work transfer in this zone.
- After this zone, the fluid flow direction changes which result in pressure loss. The enthalpy of the fluid decreases due to the pressure drop which finally results in a decrease in temperature.

5 Results and discussion

5.1 Experimental validation

The validation of the computational results is necessary for the reliability of the solution. There are very few experimental works reported in the open literature for cryogenic helium turboexpander operating at cryogenic temperature. The present results are validated with experimental results of high-pressure helium turboexpander with Chakravarty et al. [44] at a different rotational speed. Figure 13 illustrates the comparison of isentropic efficiency of present numerical results with the experimental analysis. It shows the reliability of numerical results at high-, medium-, and low-pressure turboexpander.

5.2 Effect of pressure variation on the flow field characteristics

The flow field and thermal characteristics of helium at high pressure and cryogenic temperature are entirely different because of random change in density and molecular viscosity of the fluid. In this regard, it is essential to distinguish the flow properties inside the turboexpander at different

Fig. 15 Pressure contours at 0.5 span

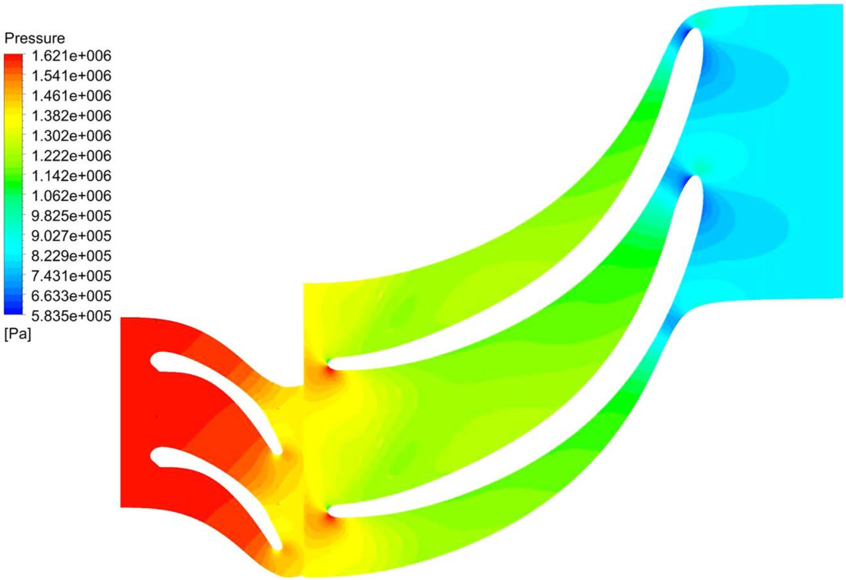

(a) High-pressure

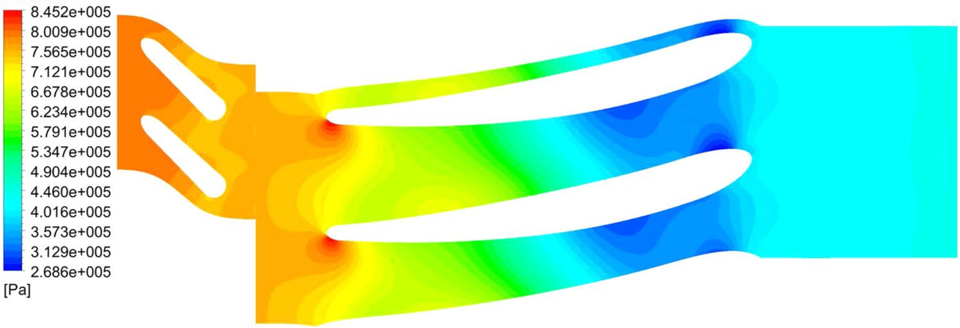

(b) Medium pressure

(c) Low pressure

operating conditions. The flow field characteristics are illustrated in the form of pressure contour, Reynolds number, Mach number, velocity vectors, etc. Additionally, the attention is extended to study the thermal behavior of the fluid such as temperature, Prandtl number, density, static enthalpy, and static entropy.

The pressure drop inside the turboexpander depends on the design of the blade profile of the nozzle and turbine. The flow must be in the subsonic regime throughout the domain. Therefore, the pressure ratio is the limiting factor to define the flow condition inside the turboexpander. Since the density of the fluid changes (Fig. 14), it must affect the quantitative variation of pressure. Under these circumstances,

Fig. 16 Mach number contours at 0.5 span

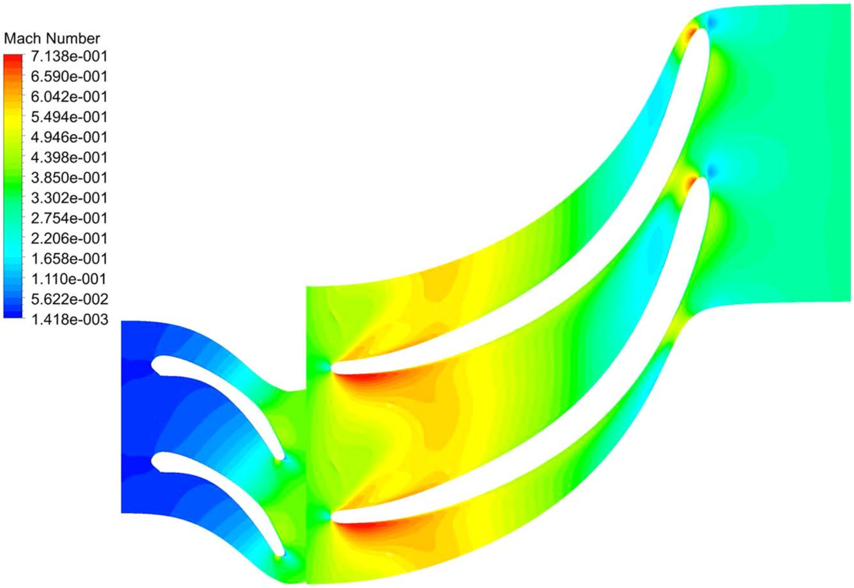

(a) High-pressure

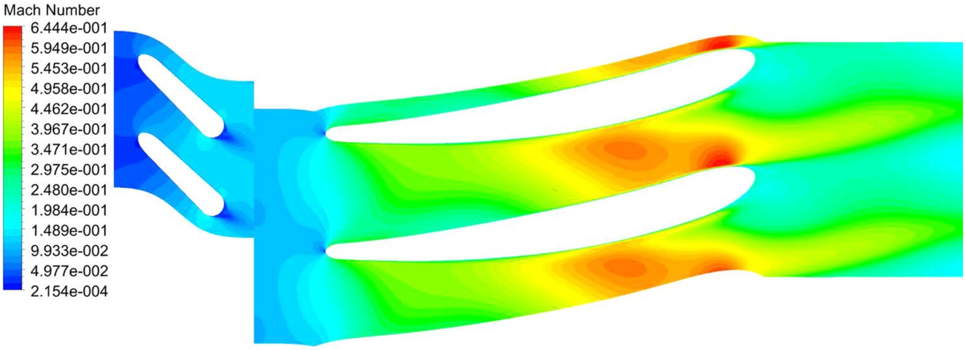

(b) Medium pressure

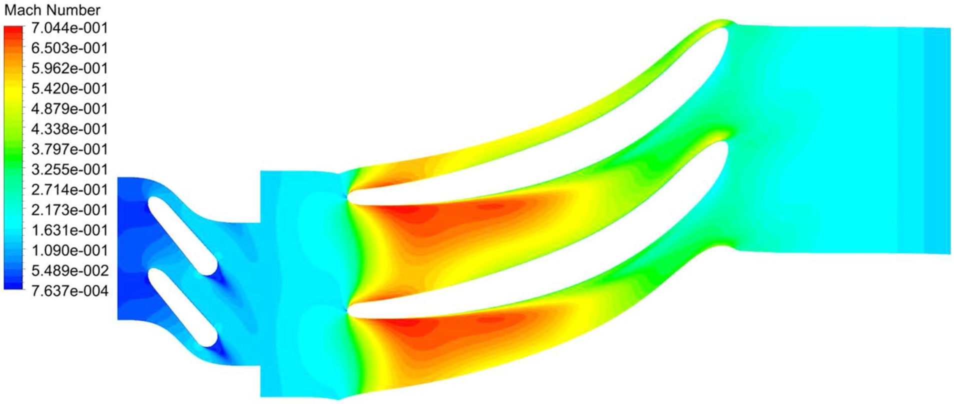

(c) Low pressure

it is essential to design three different types of turbine to overcome these effects.

Figure 15 illustrates the pressure contours of the turboexpander at 50 % span (mid-span). The nozzle is designed in such a way that the maximum pressure drop is approximately 1.2 bar. This pressure energy is converted into the kinetic energy due to which a subsonic flow regime is obtained at the nozzle exit which is essential for flow stability at the inlet of the turbine (Fig. 16). During the energy transformation process, the enthalpy decreases due to which the temperature drop takes place. The pressure ratio inside the turboexpander is approximately 2.0, 1.78, and 2.25 for high-, medium-, and low-pressure fluids, respectively. The approximate uniform pressure distribution states that the preliminary design of the

Fig. 17 Velocity vectors for high-pressure fluid

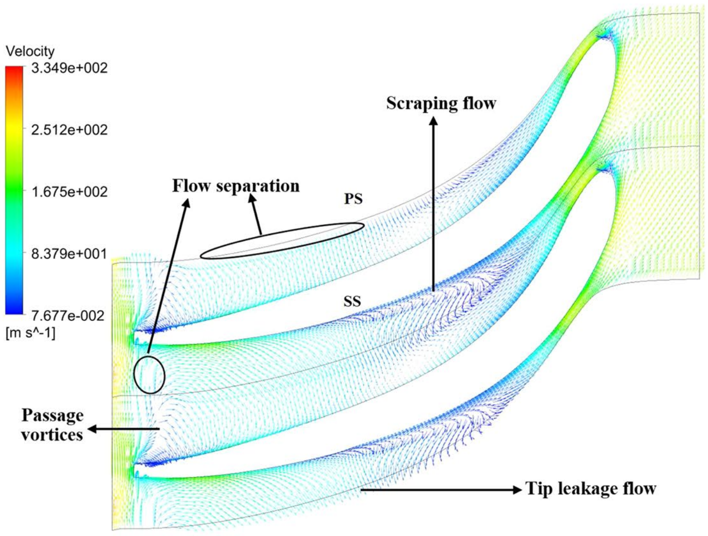

(a) Span 0.1

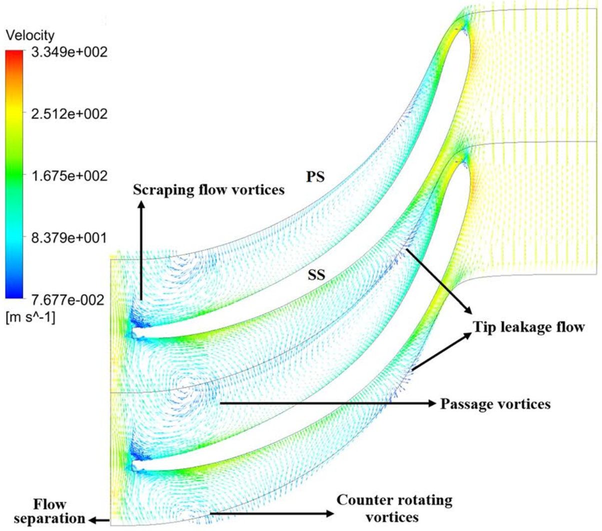

(b) Span 0.5

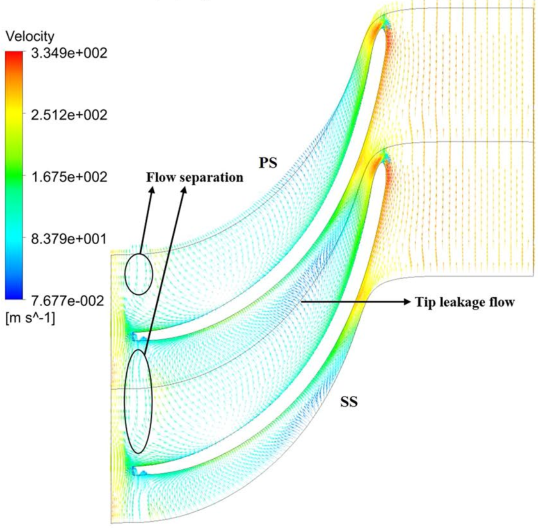

(c) Span 0.9

Fig. 18 Velocity vectors for medium-pressure fluid

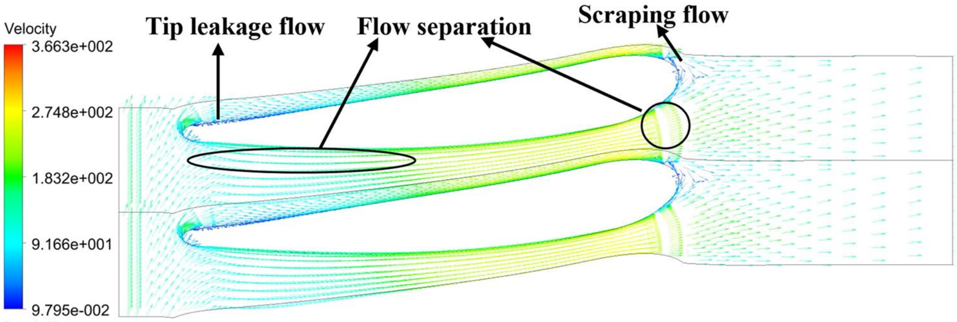

(a) Span 0.1

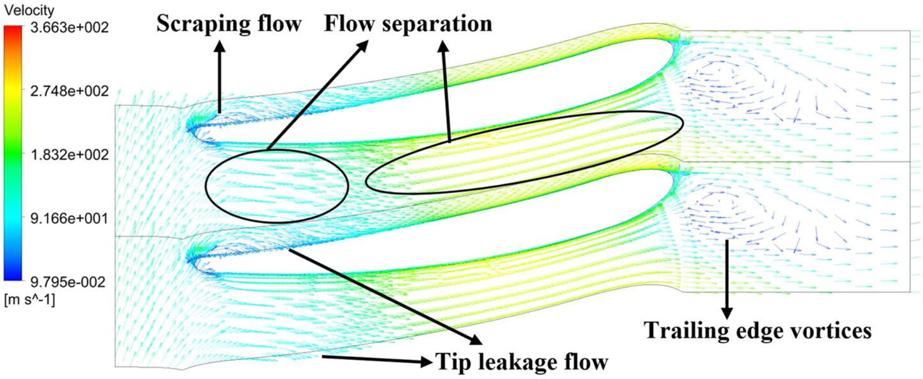

(b) Span 0.5

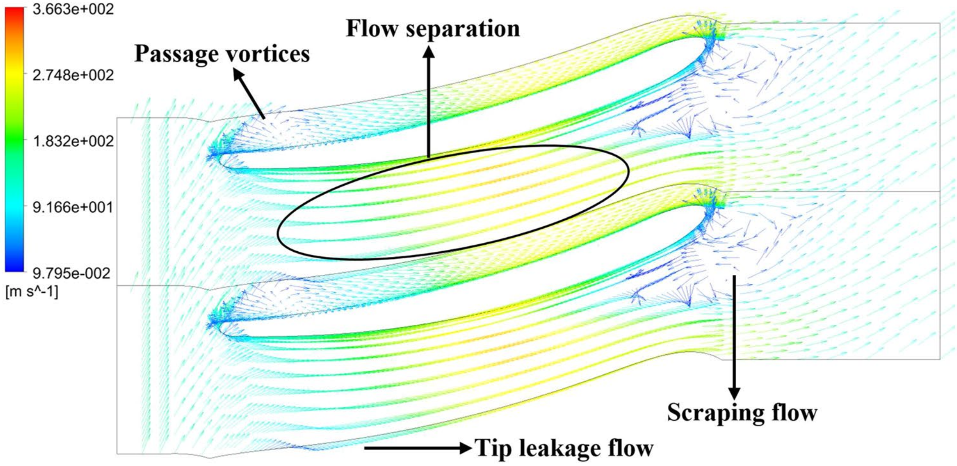

(c) Span 0.9

turboexpander is adequate for all the three models. However, some instantaneous pressure drop near the trailing edge is obtained due to rotation of the turbine blade.

Figures 17, 18, and 19 illustrate the velocity vectors for high-, medium-, and low-pressure turbines. It depicts the flow separation, vortex generation, scraping flow, passage vortices, tip leakage flow, and trailing edge vortices at a different span. For high-pressure fluid, it is noticed that the flow separation takes place at the pressure surface and passage vortices appear at 0.2 span. The adverse pressure gradient along the downstream direction is responsible for flow separation inside the turbine. The intensity of passage vortices are increasing at 0.5 span where it combines with the main flow and completely disappeared at the higher span. The scraping flow dominates near the leading edge which is responsible for vortex generation. The tip leakage flow is also appeared near the blade tip clearance due to the difference in pressure between pressure and the suction side. For medium-pressure fluid, flow separation occurs at the suction side. Also, small vortices are generated near the trailing edge. At higher span, the scraping flow occurs at the trailing edge. For low-pressure fluid, the vortices appear near

Fig. 19 Velocity vectors for low-pressure fluid

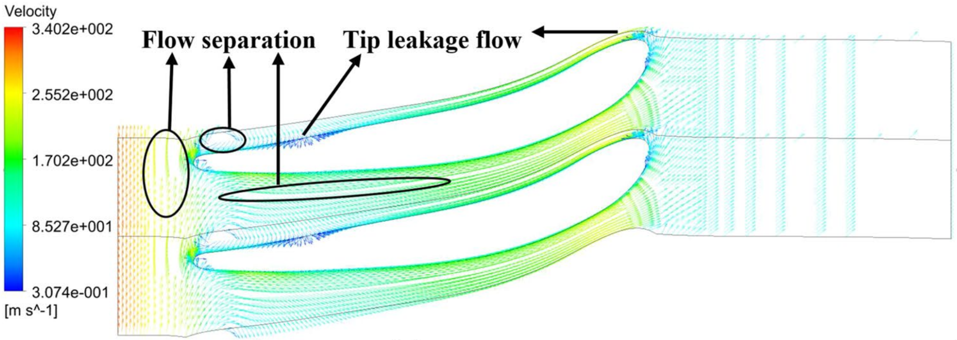

(a) Span 0.1

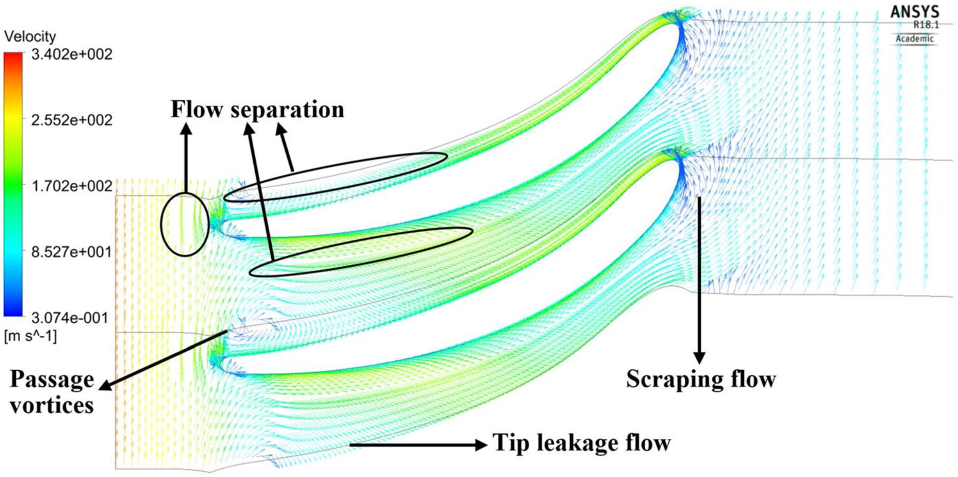

(b) Span 0.5

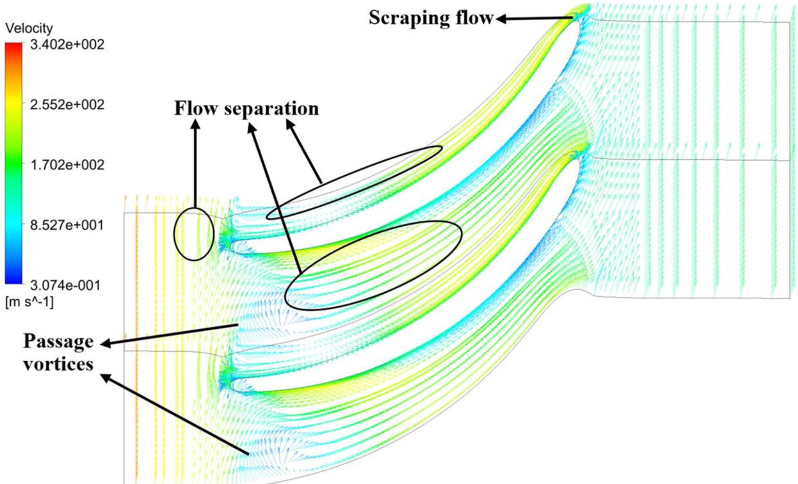

(c) Span 0.9

the leading edge. The flow separation and the intensity of vortices are relatively lower as compared to the higher span. Additionally, the secondary flow occurs in the vicinity of the blade wall boundary layer because of the relatively higher radial component of Coriolis acceleration as compared to the radial pressure gradient. This phenomenon is also observed by Zangeneh et al. [45] for the centrifugal impeller. The secondary flow also appears due to the induced pressure gradient by the curvature of the blade profile. The tip leakage flow introduces the non-uniformity and turbulence in the fluid flow and a major cause of losses in the rotating machines.

The boundary layer formation, passage vortices, free stream layer, etc. are responsible for increase in entropy. Figure 20 represents the static entropy contours at 0.5 span. The viscous friction increases due to the generation of vortices

Fig. 20 Static entropy variation for a different inlet temperature of the fluids at 0.5 span

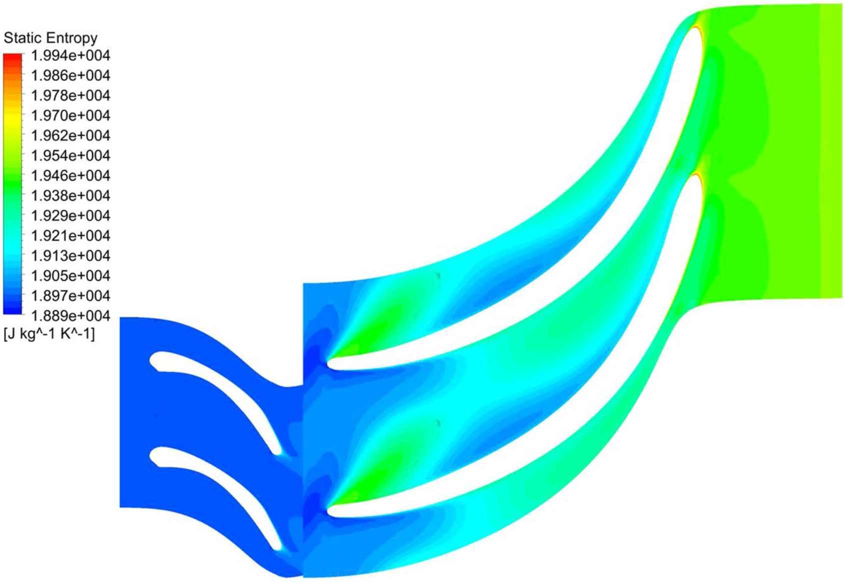

(a) High-pressure

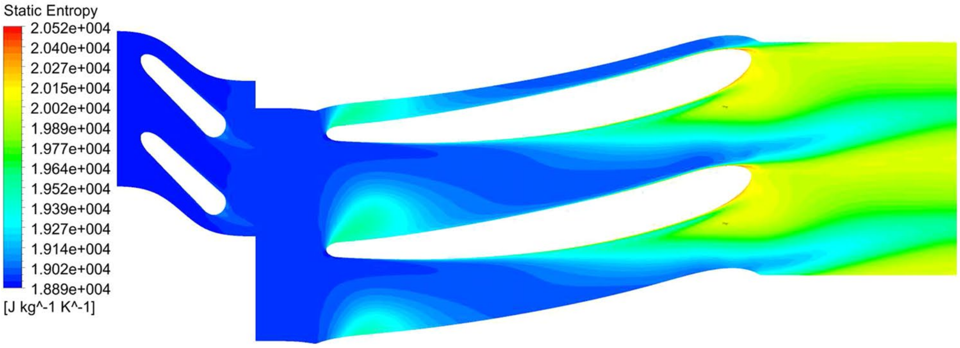

(b) Medium pressure

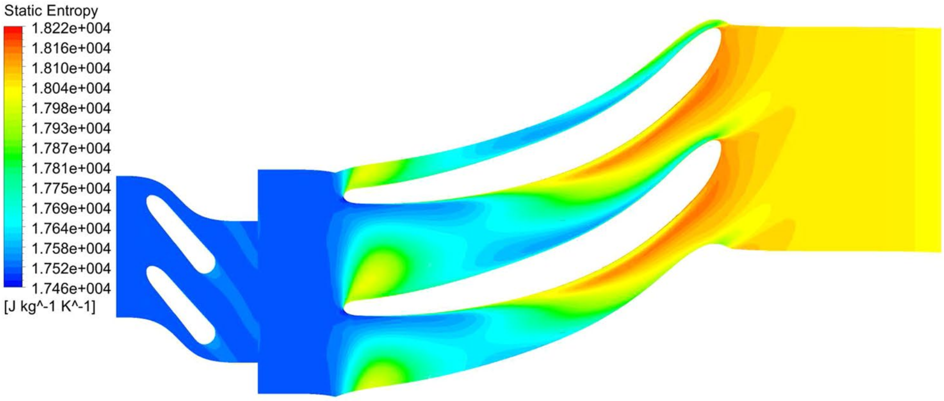

(c) Low pressure

in the flow passage which also increases the entropy of the fluid. It is also observed that the mixing of fluid streams from pressure and the suction side of the blade increases the shear strain which leads to increase in the entropy. It is noted that the entropy increases for the portion of the blade where the tip leakage flow, flow separation, and vortices are generated.

Reynolds number is defined as:

$$\mathrm{Re} = \frac{\rho v D_{\mathrm{h}}}{\mu} \tag{49}$$

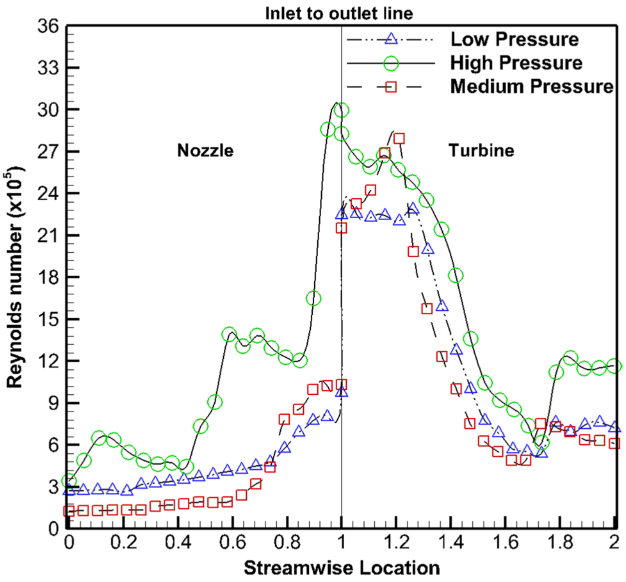

Fig. 21 Variation of Reynolds number along the streamwise location

Figure 21 illustrates the effect of the Reynolds number along with the streamwise location. The Reynolds number variation is significantly affected by hydraulic diameter, density and kinematic viscosity of the fluid. Since the low-temperature fluid approaches toward the boiling point temperature, the density increases which decreases the kinematic viscosity. It is observed that the Reynolds number is maximum for high-pressure fluid near the turbine inlet. For the remaining part, the variation is approximately similar.

5.3 Thermal characteristics

Figure 22 illustrates the temperature contours at 0.50 span. It indicates that the temperature drop for high-, medium-, and low-pressure turboexpander is 17, 14, and 12 K respectively. The temperature drop at cryogenic temperature captivates different thermal properties governed by the corresponding enthalpy drop (23a). The refrigerating capacity of the turboexpander defines the efficiency of the system. Although the phenomenon depends on the pressure drop, it also depends on the corresponding state of the fluid. The temperature drop decreases when the fluid approaches toward its boiling point. In those cases, the thermodynamic properties of the cryogenic fluids are randomly changed which severely affect the fluid flow and thermal behavior during the expansion process. The high-pressure helium has higher enthalpy as compared to the other cases. Therefore, the enthalpy drop is maximum for this case which is the major cause for a more substantial amount of temperature drop inside the turboexpander (Fig. 24). The area-averaged temperature value is computed by dividing the average temperature at the plane to the total area corresponding to that plane. In ANSYS CFX®, it is calculated in post-processing section using inlet to outlet line variation of temperature along the streamwise location of the turboexpander (Fig. 24).

The expansion of the fluid is governed by the adiabatic or throttling effect hypothesis. The law of conservation of energy states that during the expansion process, the enthalpy of the fluid decreases. For the present case, the expansion process is illustrated through the pressure-static enthalpy and temperature-static entropy variation (Fig. 25). The process irreversibility always increases the entropy of the system (Fig. 20). The ideal properties of the fluid are obtained using REFPROP which are based on the corresponding pressure and temperature of the fluid. In this regard, the isentropic efficiency $\left(\eta_{is}\right)$ is defined to consider the irreversibility of the expansion process.

The isentropic efficiency is calculated as:

$$\eta_{\mathrm{is}} = \frac{h_1 - h_3}{h_1 - h_{3,\,\mathrm{is}}} \tag{50}$$

The isentropic efficiency and power output of the system for a different inlet temperature of the fluids are mentioned in Table 11.

Prandtl number is important to specify the thermal condition of the fluid:

$$\mathrm{Pr} = \frac{\mu c_{\mathrm{p}}}{k_0} \tag{51}$$

Figure 26 illustrates the Prandtl number variation inside the turboexpander.

5.4 Effect on TKE and eddy viscosity

The turbulence intensity is quantifying in terms of TKE in turbulent flow. It can be utilized to characterize the flow effect of eddy viscosity during the fluid flow. It is not defined as a fluid property yet rather remarkably affects the flow behavior and depends on the domain and free stream parameters [42]. Since the SST model overrates the turbulence in the fluid flow which shows the magnitude of eddy diffusion and their distribution. Figure 27 illustrates the variation of TKE along the streamwise direction. It is noted that the TKE is in the lower side in the nozzle for all the cases. It happens due to the stationary component and intensity of TKE is almost identical for medium- and low-pressure fluids. For high-pressure fluid, it increases after 0.8 streamwise location. It also depicts the high-pressure fluid as the highest TKE near the rotor–stator interface. It is obvious due to high flow turbulence, and passage vortices are appeared in this zone because of the rotation effect of the turbine. The

Fig. 22 Temperature contours at 0.5 span

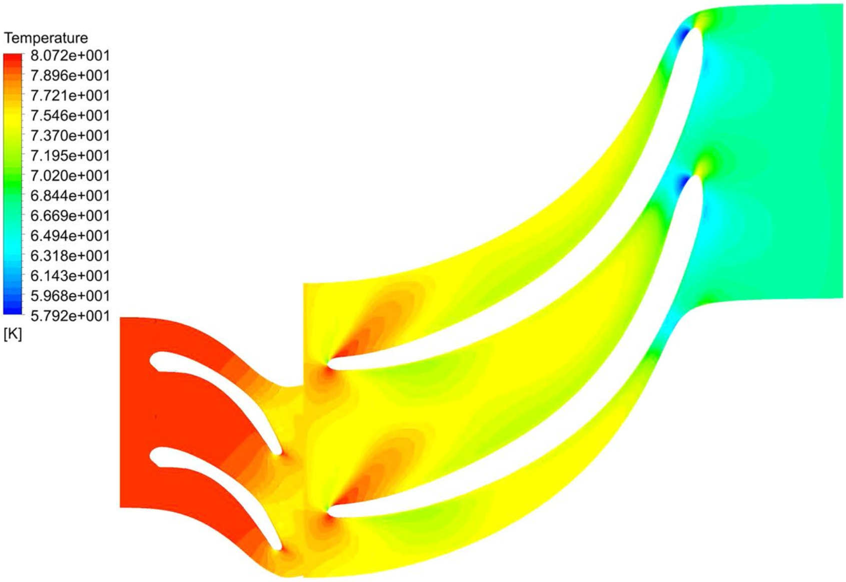

(a) High-pressure

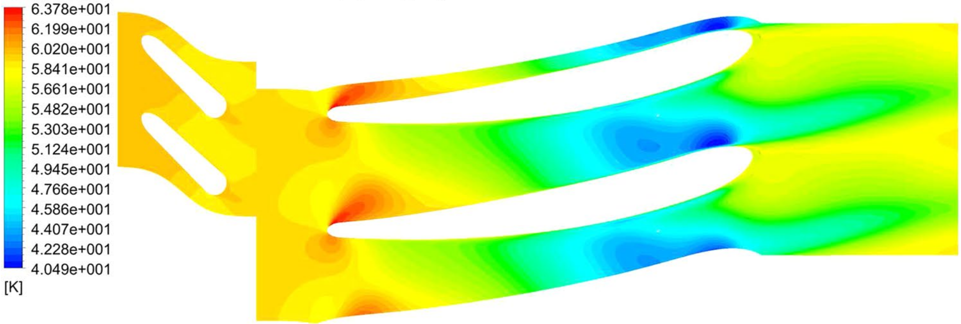

(b) Medium pressure

(c) Low pressure

medium-pressure fluid shows the highest TKE at the trailing edge which is due to the profile of the rotor blade. It can be reduced by placing the diffuser.

Figure 28 illustrates the eddy viscosity contours at 0.5 span. It is observed that the intensity of eddy viscosity is the highest near the leading edge of the rotor for high- and

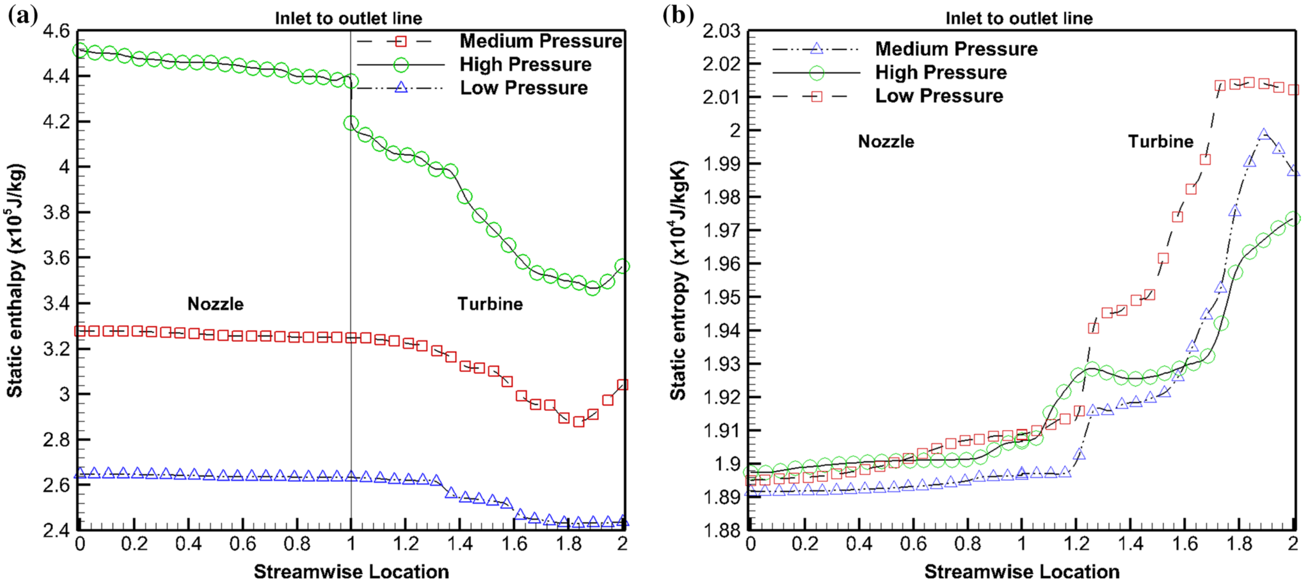

Fig. 23 Area-averaged **a** static enthalpy, **b** static entropy variation along the streamwise location

low-pressure fluids, whereas it is higher near the trailing edge for medium-pressure fluid. Generally, the intensity is increasing toward the trailing edge which is advantageous to decrease the losses incurred inside the turbine, but its appearance also depends on the domain structure.

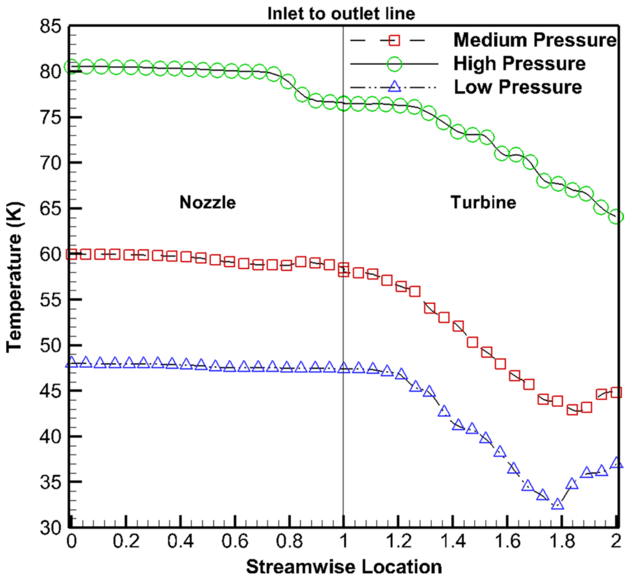

Fig. 24 Area-averaged temperature variation along the streamwise location

6 Conclusions

In this study, a comprehensive $1-D$ design methodology and performance prediction of a radial inflow turbine are demonstrated. Firstly, Sobol sensitivity analysis is performed to obtain the major non-dimensional variable. The optimal range of these variables is predicted by developing ANN and ANFIS model for better performance of the turbine. Based on these ranges, three turboexpander models are developed for numerical investigation at different operating conditions. Secondly, the numerical results are validated with the available experimental data in the open literature. After that, a comparative analysis of flow field and thermal characteristics of a helium turboexpander are explained. The analysis provides the realistic behavior of fluid flow patterns and their thermal characteristics at cryogenic temperature. Furthermore, the scraping flow, flow separation, vortices, etc. at a different span of the rotor is visualized. The study is helpful in the design and performance prediction of a cryogenic radial turbine. Additionally, the study guides to develop the experimental prototype of a helium turboexpander system. Additionally, the study assists in the development and testing of a cryogenic helium turboexpander.

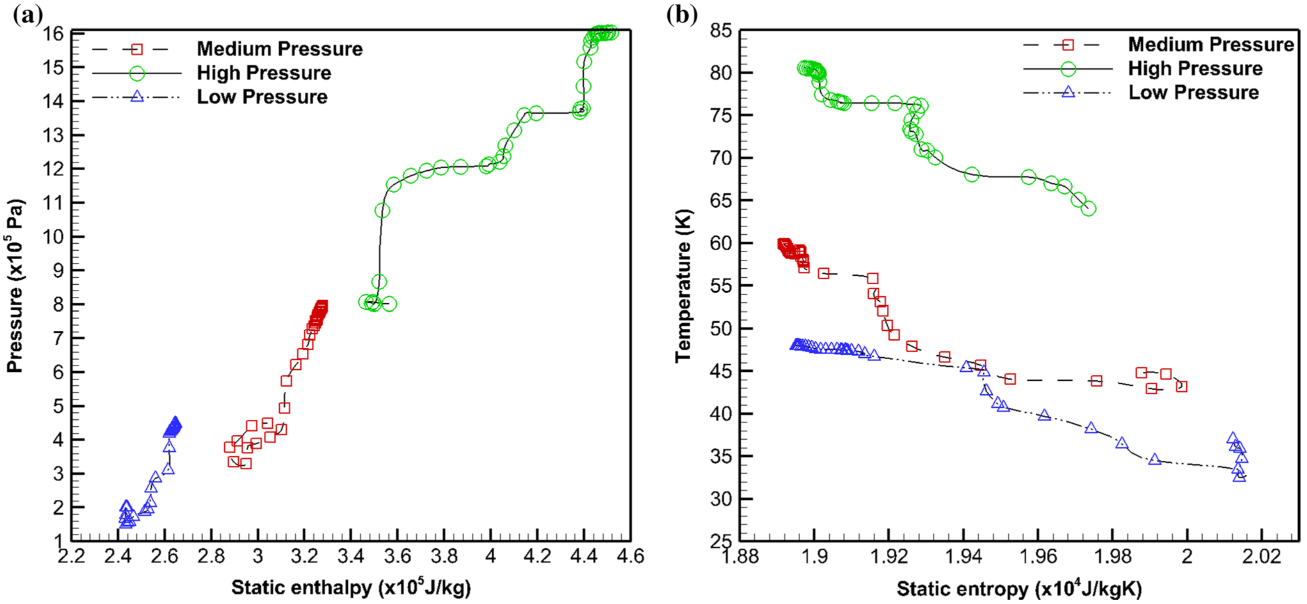

Fig. 25 **a** Pressure versus static enthalpy, **b** temperature versus static entropy variation

Table 11 Performance of the turboexpander for different operating conditions

Fluids	Isentropic efficiency (η_{is})	Power (kW)
High pressure	0.748	7.87
Medium pressure	0.785	5.24
Low pressure	0.768	6.51

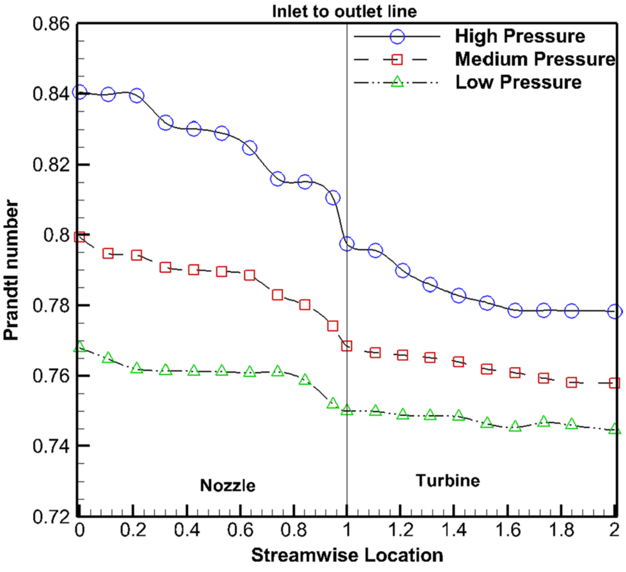

Fig. 26 Prandtl number variation along the streamwise location

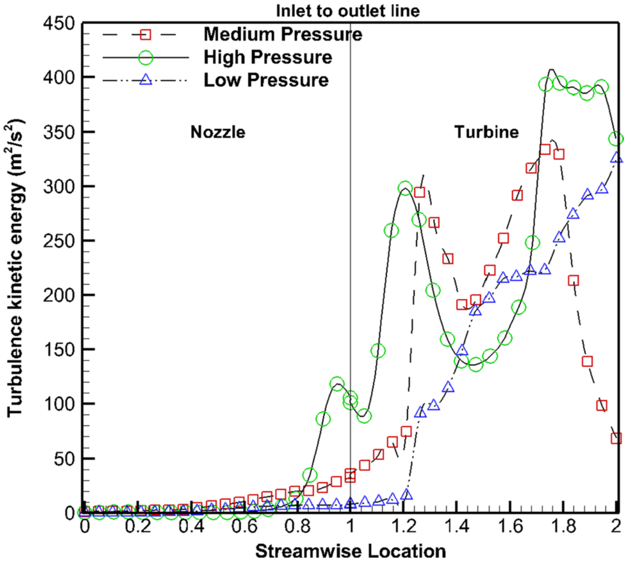

Fig. 27 Area-averaged TKE variation along the streamwise location

Fig. 28 Eddy viscosity contours at 0.5 span

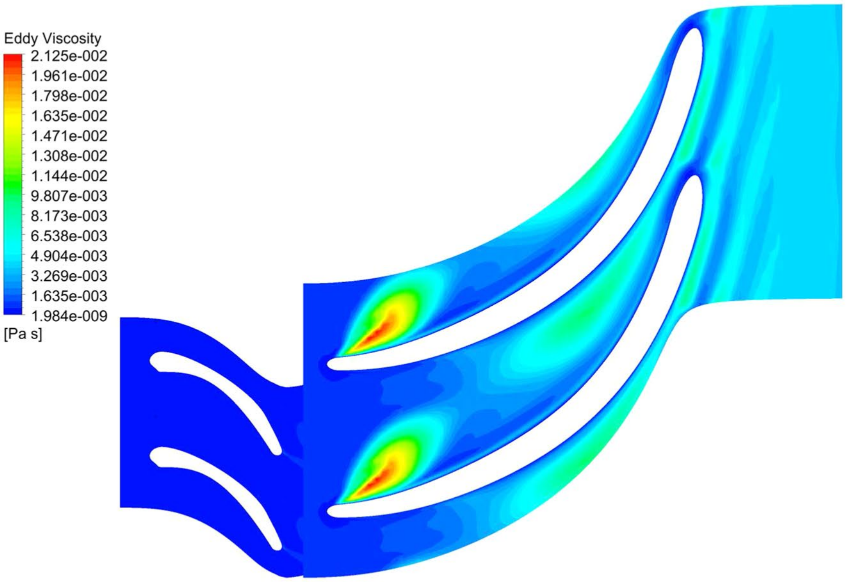

(a) High-pressure

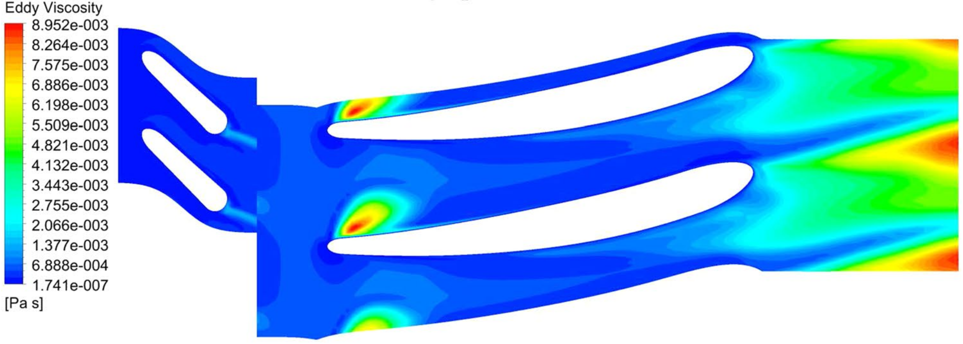

(b) Medium pressure

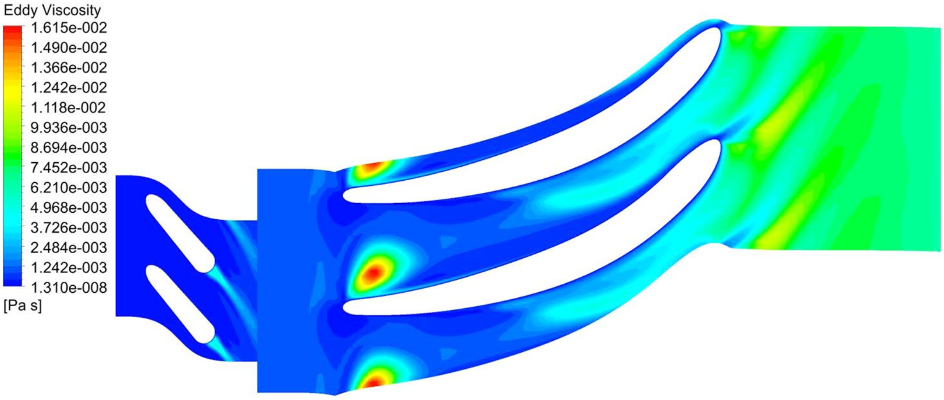

(c) Low pressure

Acknowledgements The authors sincerely thank to the Board of Research in Nuclear Sciences (BRNS) (Grant No. 39/23/2015-BRNS/39001), Ministry of Human Resource Development (MHRD), Government of India, and National Institute of Technology, Rourkela for providing the financial support.

Compliance with ethical standards

Conflict of interest The authors declared that there is no conflict of interest to any person or organization.

References

1. Mito T, Sagara A, Imagawa S, Yamada S, Takahata K, Yanagi N, Chikaraishi H, Maekawa R, Iwamoto A, Hamaguchi S et al (2006) Applied superconductivity and cryogenic research activities in NIFS. Fusion Eng Des 81(20–22):2389–2400
2. Clavel F, Alamir M, Bonnay P, Barraud A, Bornard G, Deschildre C (2011) Multivariable control architecture for a cryogenic test facility under high pulsed loads: model derivation, control design and experimental validation. J Process Control 21(7):1030–1039
3. Hall C, Dixon SL (2013) Fluid mechanics and thermodynamics of turbomachinery. Butterworth-Heinemann, Oxford
4. Wilson DG, Korakianitis T (2014) The design of high-efficiency turbomachinery and gas turbines. MIT Press, Cambridge
5. Meroni A, Robertson M, Martinez-Botas R, Haglind F (2018) A methodology for the preliminary design and performance prediction of high-pressure ratio radial-inflow turbines. Energy 164:1062–1078
6. Da Lio L, Manente G, Lazzaretto A (2017) A mean-line model to predict the design efficiency of radial inflow turbines in organic Rankine cycle (ORC) systems. Appl Energy 205:187–209
7. Aungier RH (2006) Aerodynamic design and performance analysis of exhaust diffusers. ASME Press, New York
8. Ino N, Machida A, Ttsugawa K, Arai Y, Matsuki M, Hashimoto H, Yasuda A (1992) Development of high expansion ratio helium turboexpander. In: Advances in cryogenic engineering. Springer, New York, pp 835–844
9. Ghosh SK (2008) Experimental and computational studies on cryogenic turboexpander. Ph.D. thesis, National Institute of Technology Rourkela
10. Choudhury BK (2013) Design and construction of turboexpander based nitrogen liquefier. Ph.D. thesis
11. Larjola J (1988) ORC power plant based on high speed technology. In: Conference on high speed technology. Lappeenranta, Finland, pp 21–24
12. Kumar M, Panda D, Behera SK, Sahoo RK (2019) Experimental investigation and performance prediction of a cryogenic turboexpander using artificial intelligence techniques. In: Applied thermal engineering, No. 114273
13. Sam AA, Mondal J, Ghosh P (2017) Effect of rotation on the flow behaviour in a high-speed cryogenic microturbine used in helium applications. Int J Refrig 81:111–122
14. Pei G, Li J, Li Y, Wang D, Ji J (2011) Construction and dynamic test of a small-scale organic Rankine cycle. Energy 36(5):3215–3223
15. Li X, Lv C, Yang S, Li J, Deng B, Li Q (2019) Preliminary design and performance analysis of a radial inflow turbine for a large-scale helium cryogenic system. Energy 167:106–116
16. Islamoglu Y, Kurt A, Parmaksizoglu C (2005) Performance prediction for non-adiabatic capillary tube suction line heat exchanger: an artificial neural network approach. Energy Convers Manag 46(2):223–232
17. Ghorbanian K, Soltani M, Morad M, Ashjaee M (2005) Velocity field reconstruction in the mixing region of swirl sprays using general regression neural network. J Fluids Eng 127(1):14–23
18. Joly R, Ogaji S, Singh R, Probert S (2004) Gas-turbine diagnostics using artificial neural-networks for a high bypass ratio military turbofan engine. Appl Energy 78(4):397–418
19. Ghorbanian K, Gholamrezaei M (2009) An artificial neural network approach to compressor performance prediction. Appl Energy 86(7–8):1210–1221
20. Moraal P, Kolmanovsky I (1999) Turbocharger modeling for automotive control applications. Technical report, SAE technical paper
21. Chang Y-Z, Hung K-T, Shih H-Y (2008) Optimizing the swiss-roll recuperator of an innovative micro gas turbine by a surrogate neural network and the multi-objective direct algorithm. In: ASME Turbo Expo 2008: power for land, sea, and air. American Society of Mechanical Engineers, pp 713–721
22. Yu Y, Chen L, Sun F, Wu C (2007) Neural-network based analysis and prediction of a compressor's characteristic performance map. Appl Energy 84(1):48–55
23. Fast M, Assadi M, De S (2009) Development and multi-utility of an ANN model for an industrial gas turbine. Appl Energy 86(1):9–17
24. Bartolini C, Caresana F, Comodi G, Pelagalli L, Renzi M, Vagni S (2011) Application of artificial neural networks to micro gas turbines. Energy Convers Manag 52(1):781–788
25. Mesbahi E, Assadi M, Torisson T, Lindquist T (2001) A unique correction technique for evaporative gas turbine (evgt) arameters. In: ASME Turbo Expo 2001: power for land, sea, and air. American Society of Mechanical Engineers, pp V004T04A001–V004T04A001
26. Kong C, Ki J (2007) Components map generation of gas turbine engine using genetic algorithms and engine performance Deck data. J Eng Gas Turbines Power 129(2):312–317
27. Kong C, Kho S, Ki J (2004) Component map generation of a gas turbine using genetic algorithms. In: ASME Turbo Expo 2004: power for land, sea, and air. American Society of Mechanical Engineers, pp 469–474
28. Pasquale D, Ghidoni A, Rebay S (2013) Shape optimization of an organic Rankine cycle radial turbine nozzle. J Eng Gas Turbines Power 135(4):042308
29. Harinck J, Pasquale D, Pecnik R, van Buijtenen J, Colonna P (2013) Performance improvement of a radial organic Rankine cycle turbine by means of automated computational fluid dynamic design. Proc Inst Mech Eng Part A J Power Energy 227(6):637–645
30. Sam AA, Ghosh P (2017) Flow field analysis of high-speed helium turboexpander for cryogenic refrigeration and liquefaction cycles. Cryogenics 82:1–14
31. Renu K, Bora NV (2014) Design of helium cryogenic turboexpander. Int J Sci Res Dev 1(11):2321-0613
32. Li S, Krivitzky EM, Qiu X (2016) Meanline modeling of a radial-inflow turbine nozzle with supersonic expansion. In: ASME Turbo Expo 2016: turbomachinery technical conference and exposition. American Society of Mechanical Engineers, pp V02DT42A036–V02DT42A036
33. Sauret E (2012) Open design of high pressure ratio radial-inflow turbine for academic validation. In: ASME 2012 international mechanical engineering congress and exposition. American Society of Mechanical Engineers, pp 3183–3197
34. Li Y, Ren X-D (2016) Investigation of the organic Rankine cycle (ORC) system and the radial-inflow turbine design. Appl Thermal Eng 96:547–554
35. Yang H, Wen J, Wang S, Li Y, Tu J, Cai W (2017) Sobol sensitivity analysis for governing variables in design of a plate-fin heat exchanger with serrated fins. Int J Heat Mass Transf 115:871–881
36. Wang X, Zou Z (2019) Uncertainty analysis of impact of geometric variations on turbine blade performance. Energy 176:67–80
37. Jang J-S, Sun C-T (1995) Neuro-fuzzy modeling and control. Proc IEEE 83(3):378–406
38. Schlechtingen M, Santos IF, Achiche S (2013) Using data-mining approaches for wind turbine power curve monitoring: a comparative study. IEEE Trans Sustain Energy 4(3):671–679
39. Chen Z, Choi Y-D (2015) Influence of air supply on the performance and internal flow characteristics of a cross flow turbine. Renew Energy 79:103–110
40. Dong B, Xu G, Li T, Quan Y, Zhai L, Wen J (2018) Numerical prediction of velocity coefficient for a radial-inflow turbine stator using R123 as working fluid. Appl Thermal Eng 130:1256–1265

41. Lei Q, Zhengping Z, Huoxing L, Wei L (2010) Upstream wake-secondary flow interactions in the endwall region of high-loaded turbines. Comput Fluids 39(9):1575–1584
42. Kumar M, Sahoo R, Behera S (2018) Design and numerical investigation to visualize the fluid flow and thermal characteristics of non-axisymmetric convergent nozzle. Int J Eng Sci Technol 22(1):294–312
43. Lakshminarayana B (1995) Fluid dynamics and heat transfer of turbomachinery. Wiley, New York
44. Chakravarty A (2011) Recent developments in high speed cryogenic turboexpanders at BARC, Mumbai. In: Asian conference on applied superconductivity and cryogenics, New Delhi
45. Zangeneh M, Goto A, Harada H (1998) On the design criteria for suppression of secondary flows in centrifugal and mixed flow impellers. J Turbomach 120(4):723–735